The Astronomical Journal, 133:2222–2241, 2007 May

CLUSTERING OF HIGH-REDSHIFT ($z \geq 2.9$) QUASARS FROM THE SLOAN DIGITAL SKY SURVEY

Yue Shen,[1] Michael A. Strauss,[1] Masamune Oguri,[1,2] Joseph F. Hennawi,[3] Xiaohui Fan,[4] Gordon T. Richards,[5] Patrick B. Hall,[6] James E. Gunn,[1] Donald P. Schneider,[7] Alexander S. Szalay,[8] Anirudda R. Thakar,[8] Daniel E. Vanden Berk,[7] Scott F. Anderson,[9] Neta A. Bahcall,[1] Andrew J. Connolly,[10] and Gillian R. Knapp[1]

Received 2006 November 3; accepted 2007 January 30

ABSTRACT

We study the two-point correlation function of a uniformly selected sample of 4426 luminous optical quasars with redshift $2.9 \leq z \leq 5.4$ selected over 4041 deg^2 from the Fifth Data Release of the Sloan Digital Sky Survey. We fit a power-law to the projected correlation function $w_p(r_p)$ to marginalize over redshift-space distortions and redshift errors. For a real-space correlation function of the form $\xi(r) = (r/r_0)^{-\gamma}$, the fitted parameters in comoving coordinates are $r_0 = 15.2 \pm 2.7\ h^{-1}$ Mpc and $\gamma = 2.0 \pm 0.3$, over a scale range $4\ h^{-1}$ Mpc $\leq r_p \leq 150\ h^{-1}$ Mpc. Thus high-redshift quasars are appreciably more strongly clustered than their $z \approx 1.5$ counterparts, which have a comoving clustering length $r_0 \approx 6.5\ h^{-1}$ Mpc. Dividing our sample into two redshift bins, $2.9 \leq z \leq 3.5$ and $z \geq 3.5$, and assuming a power-law index $\gamma = 2.0$, we find a correlation length of $r_0 = 16.9 \pm 1.7\ h^{-1}$ Mpc for the former and $r_0 = 24.3 \pm 2.4\ h^{-1}$ Mpc for the latter. Strong clustering at high redshift indicates that quasars are found in very massive, and therefore highly biased, halos. Following Martini & Weinberg, we relate the clustering strength and quasar number density to the quasar lifetimes and duty cycle. Using the Sheth & Tormen halo mass function, the quasar lifetime is estimated to lie in the range ~4–50 Myr for quasars with $2.9 \leq z \leq 3.5$, and ~30–600 Myr for quasars with $z \geq 3.5$. The corresponding duty cycles are ~0.004–0.05 for the lower redshift bin and ~0.03–0.6 for the higher redshift bin. The minimum mass of halos in which these quasars reside is $(2\text{–}3) \times 10^{12}\ h^{-1}\ M_\odot$ for quasars with $2.9 \leq z \leq 3.5$ and $(4\text{–}6) \times 10^{12}\ h^{-1}\ M_\odot$ for quasars with $z \geq 3.5$; the effective bias factor $b_{\rm eff}$ increases with redshift, e.g., $b_{\rm eff} \sim 8$ at $z = 3.0$ and $b_{\rm eff} \sim 16$ at $z = 4.5$.

Key words: cosmology: observations — large-scale structure of universe — quasars: general — surveys

Online material: color figures, machine-readable table

1. INTRODUCTION

Recent galaxy surveys (e.g., the 2dF Galaxy Redshift Survey [Colless et al. 2001] and the Sloan Digital Sky Survey [SDSS; York et al. 2000]) have provided ample data for the study of the large-scale distribution of galaxies in the present-day universe. The clustering of galaxies, which are tracers of the underlying dark matter distribution, gives a powerful test of hierarchical structure formation theory, especially when compared with fluctuations in the cosmic microwave background. Indeed, the results show excellent agreement with the now-standard flat Λ-dominated concordance cosmology (e.g., Spergel et al. 2003, 2007; Tegmark et al. 2004, 2006; Eisenstein et al. 2005; Percival et al. 2007). The galaxy two-point correlation function is well fit by a power law $\xi(r) = (r/r_0)^{-\gamma}$ on scales $r \lesssim 20\ h^{-1}$ Mpc, with comoving correlation length $r_0 \sim 5\ h^{-1}$ Mpc and slope $\gamma \sim 1.8$ (Totsuji & Kihara 1969; Groth & Peebles 1977; Davis & Peebles 1983; Hawkins et al. 2003), although there is an excess above the power law below $2\ h^{-1}$ Mpc, thought to be due to halo occupation effects (Zehavi et al. 2004, 2005).

At high redshifts and earlier times, the dark matter clustering strength should be weaker, but the first clustering studies of high-redshift galaxies with the Keck telescope (Cohen et al. 1996; Steidel et al. 1998; Giavalisco et al. 1998; Adelberger et al. 1998) showed that galaxies at $z > 3$ show a similar comoving correlation length to those of today, results that have since been confirmed with much larger samples (e.g., Adelberger et al. 2005b; Ouchi et al. 2005; Kashikawa et al. 2006; Meneux et al. 2006; Lee et al. 2006; Quadri et al. 2006). This is indeed expected: high-redshift galaxies are thought to form at rare peaks in the density field, which will be strongly biased relative to the dark matter (Kaiser 1984; Bardeen et al. 1986); under gravitational instability, the bias of galaxies drops over time as a function of redshift (Tegmark & Peebles 1998; Blanton et al. 2000; Weinberg et al. 2004).

Luminous quasars offer a different probe of the clustering of galaxies at high redshift. Powered by gas accretion onto central supermassive black holes (Salpeter 1964; Lynden-Bell 1969), quasars are believed to be the progenitors of local dormant supermassive black holes which are ubiquitous in the centers of nearby bulge-dominated galaxies (e.g., Kormendy & Richstone 1995; Magorrian et al. 1998; Yu & Tremaine 2002). Studies of the clustering properties of quasars date back to Osmer (1981); in general, quasars have a clustering strength similar to that of luminous galaxies at the same redshift (Shaver 1984; Croom & Shanks 1996; Porciani et al. 2004, hereafter PMN04; Croom et al. 2005). If the triggering of quasar activity is not tied to the larger scale environment in

[1] Princeton University Observatory, Princeton, NJ 08544, USA.
[2] Kavli Institute for Particle Astrophysics and Cosmology, Stanford University, Menlo Park, CA 94025, USA.
[3] Department of Astronomy, University of California, Berkeley, CA 94720, USA.
[4] Steward Observatory, Tucson, AZ 85721, USA.
[5] Department of Physics, Drexel University, Philadelphia, PA 19104, USA.
[6] Department of Physics and Astronomy, York University, Toronto, ON M3J 1P3, Canada.
[7] Department of Astronomy and Astrophysics, Pennsylvania State University, University Park, PA 16802, USA.
[8] Center for Astrophysical Sciences, Department of Physics and Astronomy, Johns Hopkins University, Baltimore, MD 21218, USA.
[9] Department of Astronomy, University of Washington, Seattle, WA 98195, USA.
[10] Department of Physics and Astronomy, University of Pittsburgh, Pittsburgh, PA 15260, USA.

which their host galaxies reside, this is not a surprising result; quasars are interpreted as a stochastic process through which every luminous galaxy passes, and therefore the clustering of quasars should be no different from that of luminous galaxies. Studies of the clustering of galaxies around quasars similarly find that quasar environments are similar to those of luminous galaxies (Serber et al. 2006 and references therein), although evidence for an enhanced clustering of quasars on small scales (Djorgovski 1991; Hennawi et al. 2006a; but see also Myers et al. 2007b) suggests that tidal effects within 100 kpc may trigger quasar activity.

A number of studies have examined the redshift evolution of quasar clustering, but the results have been controversial: some papers conclude that quasar clustering either decreases or weakly evolves with redshift (e.g., Iovino & Shaver 1988; Croom & Shanks 1996), while others say that it increases with redshift (e.g., Kundic 1997; La Franca et al. 1998; PMN04; Croom et al. 2005). Myers et al. (2006, 2007a, 2007b) examined the clustering of quasar candidates with photometric redshifts from the SDSS; they find little evidence for evolution in clustering strength between $z \approx 2$ and today. These studies also find little evidence for a strong luminosity dependence of the quasar correlation function (e.g., Croom et al. 2005; A. J. Connolly et al. 2007, in preparation), which is in accord with quasar models in which quasar luminosity is only weakly related to black hole mass (Lidz et al. 2006).

The vast majority of quasars in flux-limited samples such as the SDSS (and especially UV-excess surveys such as the 2dF QSO Redshift Survey; Croom et al. 2004) are at relatively low redshift, $z < 2.5$. More distant quasars are intrinsically rarer (e.g., Richards et al. 2006), and at a given luminosity are of course substantially fainter. However, we might expect high-redshift quasars to be appreciably more biased than their lower redshift counterparts. The high-redshift quasars in flux-limited samples are intrinsically luminous, and by the Eddington argument, are powered by massive ($>10^8\ M_\odot$) black holes. If the relation between black hole mass and bulge mass (Tremaine et al. 2002 and references therein), and by extension, black hole mass and dark matter halo mass (Ferrarese 2002), holds true at high redshift, then luminous quasars reside in very massive, and therefore very rare, halos at high redshift. Rare, many-σ peaks in the density field are strongly biased (Bardeen et al. 1986). Thus detection of particularly strong clustering at high redshift would allow tests of both the relationship between quasars and their host halos, and the predictions of biasing models. The rarity of the halos in which quasars reside is of course related to the observed number density of quasars and their duty cycle/lifetime. Thus, the quasar luminosity function and the quasar clustering properties can be used to constrain the average quasar lifetime t_Q (Haiman & Hui 2001; Martini & Weinberg 2001), or equivalently, the duty cycle: the fraction of time a supermassive black hole shines as a luminous quasar.

Studies to date of the clustering of high-redshift quasars have been hampered by small-number statistics. Stephens et al. (1997) and Kundic (1997) examined three $z > 2.7$ quasar pairs with comoving separations 5–10 h^{-1} Mpc in the Palomar Transit Grism Survey of Schneider et al. (1994), and estimated a comoving correlation length $r_0 \sim 17.5 \pm 7.5\ h^{-1}$ Mpc, which is 3 times higher than that of lower redshift quasars. Schneider et al. (2000) found a pair of $z = 4.25$ quasars in the SDSS separated by less than 2 h^{-1} Mpc; this single pair implies a lower limit to the correlation length of $r_0 = 12\ h^{-1}$ Mpc. Similarly, the quasar pair separated by a few Mpc at $z \sim 5$ found by Djorgovski et al. (2003) also implies strong clustering at high redshift. However, measuring a true correlation function requires large samples of quasars. At $z \sim 4$, the mean comoving distance between luminous ($M_i < -27.6$) quasars is $\sim 150\ h^{-1}$ Mpc (Fan et al. 2001; Richards et al. 2006), and thus to build up statistics on smaller scale clustering in such a sparse sample requires a very large volume. The SDSS quasar sample is the first survey of high-redshift quasars that covers enough volume to allow this measurement to be made.

This paper presents the correlation function of high-redshift ($z \geq 2.9$) quasars using the Fifth Data Release (DR5; Adelman-McCarthy et al. 2007) of the SDSS. DR5 contains $\sim$6000 quasars with redshift $z \geq 2.9$. We construct a homogeneous flux-limited sample for clustering analysis in § 2, with special focus on redshift determination in Appendix A and the angular mask of the sample in Appendix B. We present the correlation function itself in § 3, together with a discussion of its implications for quasar duty cycles and lifetimes. We conclude in § 4. Throughout the paper we use the third-year *WMAP* + all parameters[11] (Spergel et al. 2007) for the cosmological model: $\Omega_M = 0.26$, $\Omega_\Lambda = 0.74$, $\Omega_b = 0.0435$, $h = 0.71$, $n_s = 0.938$, and $\sigma_8 = 0.751$. Comoving units are used in distance measurements; for comparison with previous results, we will often quote distances in units of h^{-1} Mpc.

2. SAMPLE SELECTION

2.1. *The SDSS Quasar Sample*

The SDSS uses a dedicated 2.5 m wide-field telescope (Gunn et al. 2006) that uses a drift-scan camera with 30 2048 × 2048 CCDs (Gunn et al. 1998) to image the sky in five broad bands (*ugriz*; Fukugita et al. 1996). The imaging data are taken on dark photometric nights of good seeing (Hogg et al. 2001) and are calibrated photometrically (Smith et al. 2002; Ivezić et al. 2004; Tucker et al. 2006) and astrometrically (Pier et al. 2003), and object parameters are measured (Lupton et al. 2001; Stoughton et al. 2002). Quasar candidates (Richards et al. 2002a) for follow-up spectroscopy are selected from the imaging data using their colors, and are arranged in spectroscopic plates (Blanton et al. 2003) to be observed with a pair of double spectrographs. The quasars observed through the Third Data Release (Abazajian et al. 2005) have been cataloged by Schneider et al. (2005), while Schneider et al. (2006) extend this catalog to the DR5. In this paper, we will use results from DR5, for which spectroscopy has been carried out over 5740 deg^2. Because of the diameter of the fiber cladding, two targets on the same plate cannot be placed closer than 55″ (corresponding to $\sim 1.2\ h^{-1}$ Mpc at $z = 3$);[12] the present paper therefore concentrates on clustering on larger scales, and we will present a discussion of the correlation function on small scales in a paper in preparation.

The quasar target selection algorithm is in two parts: quasars with $z \leq 3.5$ are outliers from the stellar locus in the *ugri* color cube, while those with $z > 3.5$ are selected as outliers in the *griz* color cube. The quasar candidate sample is flux-limited to $i = 19.1$ (after correction for Galactic extinction following Schlegel et al. 1998), but because high-redshift quasars are quite rare, the magnitude limit for objects lying in those regions of color space corresponding to quasars at $z > 3$ are targeted to $i = 20.2$. The quasar locus crosses the stellar locus in color space at $z \approx 2.7$ (Fan 1999), meaning that quasar target selection is quite incomplete there (Richards et al. 2006). For this reason, we have chosen to define high-redshift quasars as those with $z \geq 2.9$.

[11] See http://lambda.gsfc.nasa.gov/product/map/current/params/lcdm_all.cfm.

[12] Serendipitous objects closer than 55″ might be observed on overlapped plates.

TABLE 1
High-Redshift Quasar Sample

Plate	Fiber	MJD	R.A. (deg)	Decl. (deg)	z	$z_{\rm err}$	i Magnitude	sub_flag	good_flag
1091	553	52902	0.193413	1.239112	3.741	0.011	19.74	0	0
1489	506	52991	0.214856	0.200710	3.881	0.030	19.97	0	0
1489	104	52991	0.397978	−0.701886	3.572	0.008	19.33	0	0
0387	556	51791	0.587972	0.363741	3.057	0.010	18.58	0	0
0650	111	52143	0.660070	−10.197168	3.942	0.012	19.97	0	0
0750	608	52235	0.751425	16.007709	3.689	0.011	19.50	1	1
0650	048	52143	0.763943	−10.864079	3.645	0.011	19.20	0	0
0750	036	52235	0.896718	14.795454	3.462	0.012	19.95	1	1
0750	632	52235	1.155146	15.174562	3.203	0.009	20.17	1	1
0751	207	52251	1.401625	13.997071	3.705	0.011	19.34	1	1

Notes.—The entire high-redshift quasar sample with duplicate objects removed. The sub_flag is 1 when an object is in the clustering subsample, and the good_flag is 1 for objects lying in good fields. The i magnitudes are SDSS PSF (asinh) magnitudes corrected for Galactic extinction (Schlegel et al. 1998); they use the ubercalibration described by N. Padmanabhan et al. (2007, in preparation), which differs slightly from that used in the official DR5 quasar catalog (Schneider et al. 2006). Table 1 is published in its entirety in the electronic edition of the *Astronomical Journal*. A portion is shown here for guidance regarding its form and content.

We draw our parent sample from the SDSS DR5 catalog. We have taken all quasars with listed redshift $z \geq 2.9$ from the DR3 quasar catalog (Schneider et al. 2005); the redshifts of these objects have all been checked by eye, and we rectify a small number of incorrect redshifts in the database. This sample contains 3333 quasars. In addition, we have included all objects on plates taken since DR3 with listed redshift $z \geq 2.9$ as determined either from the official spectroscopic pipeline that determines redshifts by measuring the position of emission lines (SubbaRao et al. 2002) or an independent pipeline that fits spectra to quasar templates (D. J. Schlegel et al. 2007, in preparation). We examined by eye the spectra of all objects with discrepant redshifts between the two pipelines. There are 2805 quasars added to our sample from plates taken since DR3.

Quasar emission lines are broad and tend to show systematic wavelength offsets from the true redshift of the object (Richards et al. 2002b and references therein). Appendix A describes our investigation of these effects, the determination of an unbiased redshift for each object, and the definition of our final sample of 6109 quasars with $z \geq 2.9$ (after rejecting 29 objects that turn out to have $z < 2.9$).

2.2. *Clustering Subsample*

Not all the quasars in our sample are suitable for a clustering analysis. Here we follow Richards et al. (2006) and select only those quasars that are selected from a uniform algorithm. In particular:

1. The version of the quasar target selection algorithm used for the SDSS Early Data Release (Stoughton et al. 2002) and the First Data Release (DR1; Abazajian et al. 2003) did a poor job of selecting objects with $z \approx 3.5$. We use only those quasars targeted with the improved version of the algorithm, i.e., those with target selection version no lower than v3_1_0.
2. Some quasars are found using algorithms other than the quasar target selection algorithm described by Richards et al. (2002a), including special selection in the southern Galactic cap (see Adelman-McCarthy et al. 2006) and optical counterparts to *ROSAT* sources (Anderson et al. 2003). The completeness of these auxiliary algorithms is poor, and we only include quasars targeted by the main algorithm.
3. Because quasars are selected by their optical colors, regions of sky in which the SDSS photometry is poor are unlikely to have complete quasar targeting.

We now describe how the regions with poor photometry are identified. The SDSS images are processed in a series of $10' \times 13'$ *fields*. We follow Richards et al. (2006) and mark a given field as having bad photometry if any one of the following criteria is satisfied:

1. The r-band seeing is greater than $2.0''$.
2. The operational database quality flag for that field is BAD, MISSING, or HOLE (only 0.15% of all DR5 fields have one of these flags set).
3. The median difference between the PSF and large-aperture photometry magnitudes of bright stars lies more than 3 σ from the mean over the entire DR5 sample in any of the five bands.
4. Any of the four principal colors of the stellar locus (Ivezić et al. 2004) deviates from the mean of the DR5 sample by more than 3 σ.
5. Any of the four values of the rms scatter around the mean principal color deviates from the mean over DR5 by more than 5 σ, or deviates from the DR5 mean by more than 2 σ and also deviates from the mean of that *run* by more than 3 σ. This criterion reflects the fact that the statistics of the rms widths of the principal color distributions per field vary significantly from run to run.

All the information we need to identify bad fields in this way can be retrieved from the runQA table in the SDSS Catalogue Archive Server (CAS).[13] A total of 13.24% of the net area of the clustering subsample is marked as bad. These bad fields will serve as a secondary mask in our geometry description. We will compute the correlation function both including and excluding the bad regions, to test our sensitivity to possible selection problems in the bad regions.

Finally, due to overlapping plates, there are roughly 200 duplicate objects in our parent sample, which we identified and removed using objects' positions.

Our final cleaned subsample contains 4426 quasars before excluding bad fields and 3846 quasars with bad fields excluded. Thus 13.1% of high-redshift quasars are in bad fields, essentially identical to the fraction of the area flagged as bad, which suggests that the selection of quasars in these regions is not terribly biased. A list of the unique high-redshift quasars in our parent sample and in the subsample used in our clustering analysis is provided in Table 1.

[13] See http://cas.sdss.org.

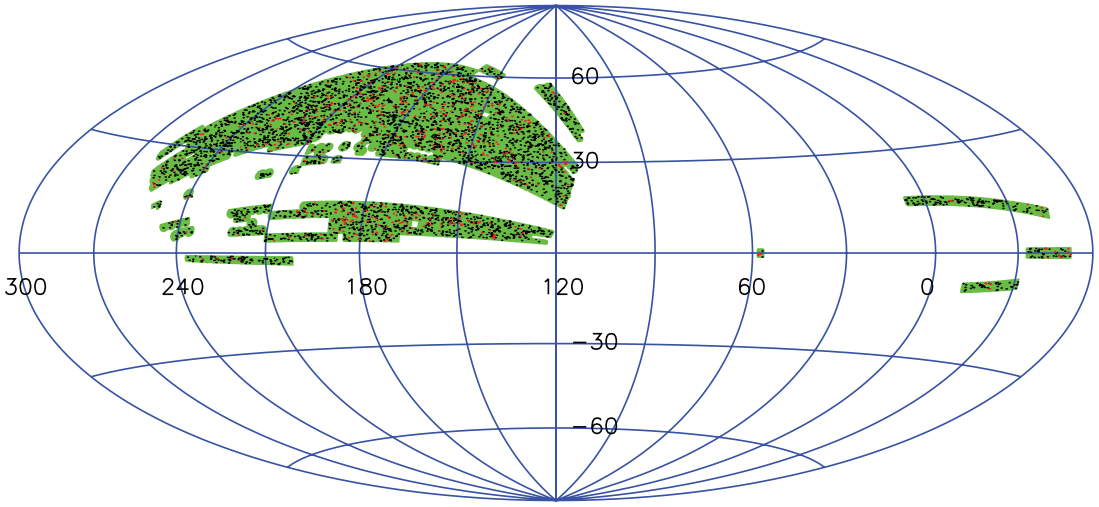

FIG. 1.—Aitoff projection in equatorial coordinates of the angular coverage of our clustering subsample (with all fields). The center of the plot is the direction R.A. = 120° and decl. = 0°. The dots indicate quasars in our clustering subsample, with red dots indicating those in bad imaging fields. The angular coverage is patchy due to the various selection criteria described in § 2.2 and Appendix B. For example, much of the southern equatorial stripe ($\delta = 0$, $300° < \alpha < 60°$) was targeted using the old version of the quasar targeting algorithm.

2.3. *Distribution of Quasars in Angle and on the Sky*

The footprint of our quasar clustering subsample is quite complicated. The definition of the sample's exact boundaries, needed for the correlation function analysis which follows, is described in detail in Appendix B. Figure 1 shows the area of sky from which the sample was selected in green, and the sample of quasars is indicated as dots, with red dots indicating objects in bad imaging fields. The total area subtended by the sample is 4041 deg^2; when bad fields are excluded, the solid angle drops to 3506 deg^2.

The target selection algorithm for quasars is not perfect and the selection function depends on redshift. Our sample is limited to $z \geq 2.9$; at slightly lower redshift, the broadband colors of quasars are essentially identical to those of F stars (Fan 1999), giving a dramatic drop in the quasar selection function. Moreover, as discussed in Richards et al. (2006), quasars with redshift $z \approx 3.5$ have similar colors to G/K stars in the *griz* diagram and hence targeting becomes less efficient around this redshift (as mentioned above, this problem was even worse for the version of target selection used in the EDR and DR1). This is reflected in the redshift distribution of our sample (Fig. 2), which shows a dip at $z \approx 3.5$. We will use these distributions in computing the correlation function below.

3. CORRELATION FUNCTION

Now that we understand the angular and radial selection function of our sample, we are ready to compute the two-point correlation function. Doing so requires producing a random catalog of points (i.e., without any clustering signal) with the same spatial selection function. We will first compute the correlation function in "redshift space" in § 3.1, then derive the real-space correlation function in § 3.2 by projecting over redshift-space distortions. Our calculations will be done both including and excluding the bad fields (§ 2.2); we will find that our results are robust to this detail.

3.1. *"Redshift Space" Correlation Function*

We draw random quasar catalogs according to the detailed angular and radial selection functions discussed in the last section. We start by computing the correlation function in "redshift space," where each object is placed at the comoving distance implied by its measured redshift and our assumed cosmology, with no correction for peculiar velocities or redshift errors.[14] The correlation function is measured using the estimator of Landy & Szalay (1993):[15]

$$\xi_s(s) = \frac{\langle DD\rangle - 2\langle DR\rangle + \langle RR\rangle}{\langle RR\rangle}, \quad (1)$$

where $\langle DD\rangle$, $\langle DR\rangle$, and $\langle RR\rangle$ are the normalized numbers of data-data, data-random, and random-random pairs in each separation bin, respectively. The results are shown in Figure 3, where we bin

[14] All calculations in this paper are done in comoving coordinates, which is appropriate for comparing clustering results at different epochs on linear scales. On very small, virialized scales, Hennawi et al. (2006a) argue that proper coordinates are more appropriate for clustering analyses.

[15] We found that the Hamilton (1993) estimator gives similar results.

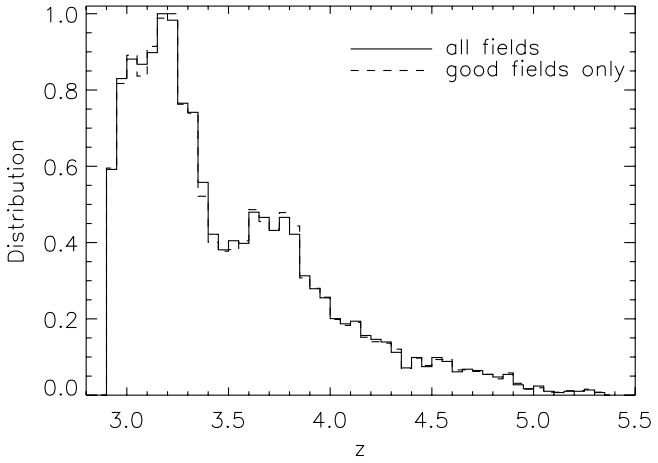

FIG. 2.—Observed redshift distribution of our quasar clustering subsamples, normalized by the peak value. This distribution is the product of the evolution of the quasar density distribution and the quasar selection function; the latter is responsible for the dip at $z \approx 3.5$, where quasars have very similar colors to those of G and K stars. We show the redshift distributions for the subsamples both including and excluding bad fields; the results are essentially identical. The redshift binning is $\Delta z = 0.05$.

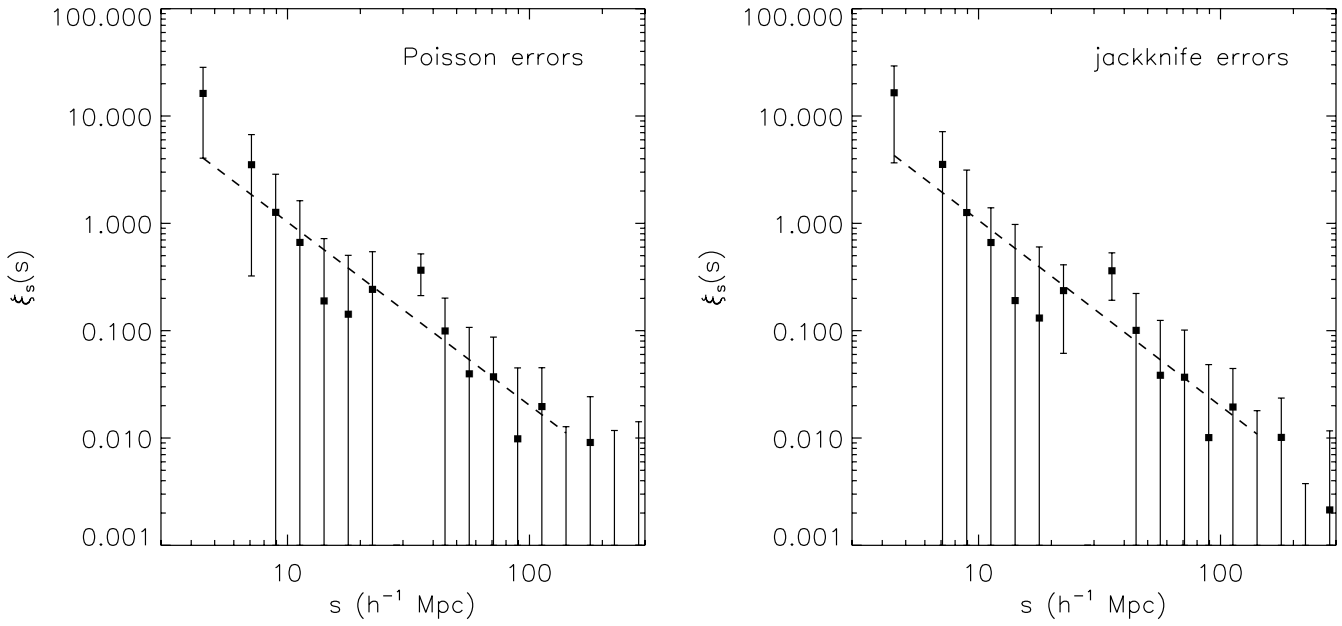

FIG. 3.—Redshift-space correlation function $\xi_s(s)$ for quasars with $z \geq 2.9$ (all fields included). Statistical errors are estimated using the Poisson estimator (*left*) and jackknife estimator (*right*). The two estimators give comparable results. Also plotted are the best-fit power-law functions, with fitted parameters listed in Table 4.

the redshift-space distance s in logarithmic intervals of $\Delta \log s = 0.1$. We tabulate the results in Table 2.

There are various ways to estimate the statistical errors in the correlation function (e.g., Hamilton 1993), including bootstrap resampling (e.g., PMN04), jackknife resampling (e.g., Zehavi et al. 2005), and the Poisson estimator (e.g., Croom et al. 2005; da Ângela et al. 2005). In this paper we will focus on the latter two methods. For the jackknife method, we split the clustering sample into 10 spatially contiguous subsamples, and our jackknife samples are created by omitting each of these subsamples in turn. Therefore, each of the jackknife samples contains 90% of the quasars, and we use each to compute the correlation function. The covariance error matrix is estimated as

$$\mathrm{Cov}(\xi_i,\ \xi_j) = \frac{N-1}{N}\sum_{l=1}^{N}\left(\xi_i^l - \bar{\xi}_i\right)\left(\xi_j^l - \bar{\xi}_j\right), \qquad (2)$$

where $N = 10$ in our case, the subscript denotes the bin number, and $\bar{\xi}_i$ is the mean value of the statistic ξ_i over the jackknife

TABLE 2
REDSHIFT-SPACE CORRELATION FUNCTION $\xi_s(s)$

s (h^{-1} Mpc)	DD_{mean}	RR_{mean}	DR_{mean}	ξ_s	ξ_s Error
2.244	0.0	0.9	0.0	...	...
2.825	0.0	5.4	0.0	...	...
3.557	0.0	6.3	0.0	...	...
4.477	1.8	14.4	0.9	16.5	12.8
5.637	0.0	34.2	3.6	...	...
7.096	1.8	38.7	11.7	3.54	3.61
8.934	1.8	99.0	18.0	1.26	1.88
11.25	2.7	215.0	36.9	0.663	0.733
14.16	4.5	406.5	80.0	0.191	0.786
17.83	8.9	804.2	162.4	0.131	0.472
22.44	15.2	1592.4	279.4	0.236	0.175
28.25	22.4	3123.6	607.3	−0.280	0.223
35.57	70.7	6028.6	1139.3	0.361	0.170
44.77	104.9	11959.1	2137.1	0.101	0.121
56.37	210.9	23480.2	4381.2	0.0384	0.0862
70.96	384.8	45648.7	8239.8	0.0368	0.0644
89.34	734.2	88337.9	16036.1	0.0101	0.0382
112.5	1417.1	168480.9	30636.2	0.0194	0.0250
141.6	2565.8	317727.8	57230.3	−0.00396	0.0219
178.3	4821.6	588892.8	106083.7	0.0101	0.0134
224.4	8631.8	1070807.1	192603.7	−0.00296	0.00672
282.5	15376.1	1912774.1	342706.1	0.00214	0.00953

NOTES.—Results for all fields. DD_{mean}, RR_{mean}, and DR_{mean} are the mean numbers of quasar-quasar, random-random, and quasar-random pairs within each s bin for the 10 jackknife samples; $\xi(s)$ is the mean value calculated from jackknife samples, and the error quoted is that from the jackknifes as well.

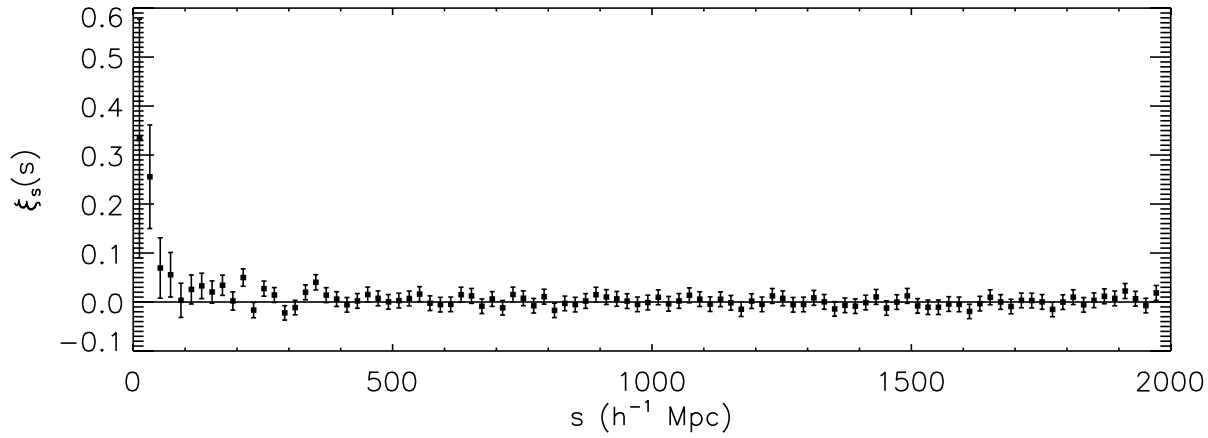

FIG. 4.—Large-scale behavior of $\xi_s(s)$ for the $z \geq 2.9$ quasars (all fields included). Errors are estimated using the Poisson estimator. The redshift-space correlation function essentially vanishes after $s > 200\ h^{-1}$ Mpc, with a mean of 0.002 and rms scatter ± 0.01 in the range $200\ h^{-1}$ Mpc $< s < 2000\ h^{-1}$ Mpc.

samples (not surprisingly, we found that $\bar{\xi}_i$ was very close to the correlation function for the whole clustering sample, for all bins i). Our sample is sparse, thus the off-diagonal elements of the covariance matrix are poorly determined, so we use only the diagonal elements of the covariance matrix in the χ^2 fits below. We also carried out fits keeping those off-diagonal elements for adjacent and separated-by-two bins, and found similar results.

For the Poisson error estimator (e.g., Kaiser 1986), valid for sparse samples in which a given quasar is unlikely to take part in more than one pair, the error is estimated as $\Delta\xi_i = (1 + \xi_i)/[\min(N_{\rm pair},\ N_{\rm QSO})]^{1/2}$, where $N_{\rm pair}$ is the number of unique quasar-quasar pairs in our real-quasar sample in the bin in question, and $N_{\rm QSO}$ is the total number of real quasars in our sample (e.g., da Ângela et al. 2005). The Poisson estimator breaks down on large scales, as the pairs in different bins become correlated. Figure 3 shows the two error estimators; the two methods give similar results.

The correlation function lies above unity for scales below $\sim 10\ h^{-1}$ Mpc; it is clear that the clustering signal is much stronger than that of low-redshift quasars (e.g., Croom et al. 2005; A. J. Connolly et al. 2007, in preparation). Figure 3 also shows the results of a χ^2 fit of a power-law correlation function $\xi_s(s) = (s/s_0)^{-\delta}$ to the data with $4\ h^{-1}$ Mpc $< s < 150\ h^{-1}$ Mpc. The clustering signal is negative in the $s = 28.25\ h^{-1}$ Mpc bin; Table 2 shows a smaller number of quasar-quasar pairs than expected. This point appears to be an outlier, as the expected correlation function should be positive on these scales; this discrepancy may be due to the paucity of quasars in the sample at $z \sim 3.5$. We have carried out fits to $\xi_s(s)$ both including and not including this data point (Table 4); we find it makes little difference. In particular, neglecting the point at $28.25\ h^{-1}$ Mpc, we find $s_0 = 10.2 \pm 3.1\ h^{-1}$ Mpc and $\delta = 1.71 \pm 0.43$ for the Poisson errors, and $s_0 = 10.4 \pm 3.0\ h^{-1}$ Mpc and $\delta = 1.73 \pm 0.46$ for the jackknife method. When we include this negative data point, we find $s_0 = 10.4\ h^{-1}$Mpc and $\delta = 2.07$ for the jackknife method. Table 4 also includes the χ^2/dof for these fits; in all cases, it is less than unity, due to our neglecting the off-diagonal elements in the covariance matrix. However, as Figure 3 makes clear, the majority of the points lie within 1 σ of the fitted power law.

Using good fields only yields similar results for bins where there are more than 20 real-quasar pairs (i.e., $s \gtrsim 20\ h^{-1}$ Mpc). On scales below $20\ h^{-1}$ Mpc there are very few quasar-quasar pairs in each bin, and the signal-to-noise ratio is very low. The fitting results (over scale range $4\ h^{-1}$ Mpc $< s < 150\ h^{-1}$ Mpc) are $s_0 = 12.7 \pm 3.3\ h^{-1}$ Mpc and $\delta = 1.64 \pm 0.31$ for the Poisson errors, and $s_0 = 10.3 \pm 3.0\ h^{-1}$ Mpc and $\delta = 1.43 \pm 0.28$ for the jackknife errors.

To study the large scale behavior of $\xi_s(s)$ we compute $\xi_s(s)$ up to $s = 2000\ h^{-1}$ Mpc on a linear grid with $\Delta s = 20\ h^{-1}$ Mpc, using all the fields. The result is shown in Figure 4 and errors are estimated using the Poisson estimator. For scales $200\ h^{-1}$ Mpc $< s < 2000\ h^{-1}$ Mpc, the mean value of $\xi_s(s)$ is 0.002, with an rms scatter of ± 0.01 (see also Roukema et al. 2002 and Croom et al. 2005). Thus there is no clear evidence for correlations on scales above $200\ h^{-1}$ Mpc.

3.2. *The Real-Space Correlation Function*

Appendix A shows that the uncertainty in measurements of the quasar redshifts is substantial, $\Delta z \approx 0.01$, giving an uncertainty in the comoving distance of a $z = 3.5$ quasar of $\sim 6\ h^{-1}$ Mpc. This, together with peculiar velocities on large and small scales, systematically biases the correlation function (e.g., Kaiser 1987). To determine the real-space correlation function, we follow standard practice and compute the correlation function on a two-dimensional grid of pair separations parallel (π) and perpendicular (r_p) to the line of sight. Our grid has a logarithmic increment of 0.15 along the r_p-direction and a linear increment of $5\ h^{-1}$ Mpc along the π-direction. As above, the two-dimensional correlation function $\xi_s(r_p,\ \pi)$ is estimated using the Landy & Szalay (1993) estimator, equation (1). Redshift errors and peculiar velocities affect the separation along the π-direction but not along the r_p-direction. Therefore we project out these effects by integrating $\xi_s(r_p,\ \pi)$ along the π-direction to obtain the projected correlation function $w_p(r_p)$:

$$w_p(r_p) = 2 \int_0^\infty d\pi\, \xi_s(r_p,\ \pi). \tag{3}$$

In practice we integrate up to some cutoff value of $\pi_{\rm cutoff} = 100\ h^{-1}$ Mpc, which includes most of the clustering signal, without being dominated by noise. This value of $\pi_{\rm cutoff}$ is larger than the values of 40–70 h^{-1} Mpc typically used in clustering analyses for galaxies and low-redshift quasars (e.g., Zehavi et al. 2005; PMN04; da Ângela et al. 2005) because of the substantially stronger clustering of high-redshift quasars. We verify that our results are not sensitive to the precise value of $\pi_{\rm cutoff}$ we adopt.

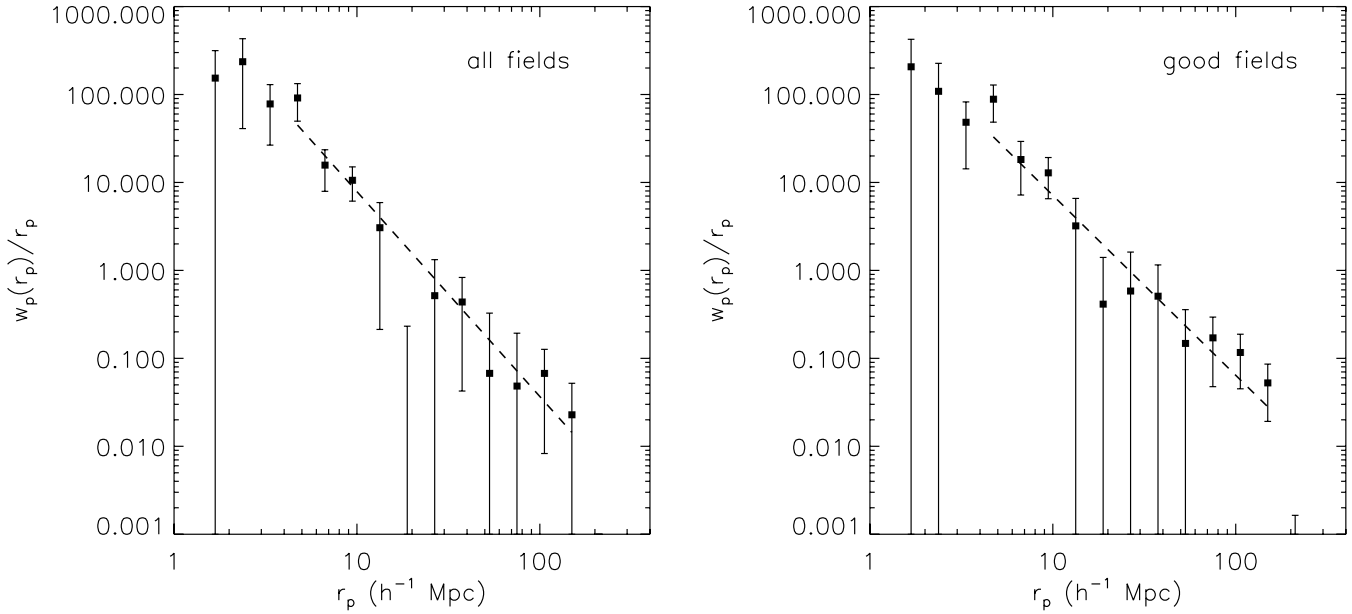

FIG. 5.—Projected correlation function $w_p(r_p)$ for the $z \geq 2.9$ quasars. Errors are estimated using the jackknife method. Also plotted are the best-fit power-law functions, with fitted parameters listed in Table 4. *Left*: All fields. *Right*: Good fields only. The two cases give similar results.

The projected correlation function w_p is related to the real-space correlation function $\xi(r)$ through

$$w_p(r_p) = 2 \int_{r_p}^{\infty} \frac{r\xi(r)}{(r^2 - r_p^2)^{1/2}} dr \qquad (4)$$

(e.g., Davis & Peebles 1983). If $\xi(r)$ follows the power-law form $\xi(r) = (r/r_0)^{-\gamma}$, then

$$\frac{w_p(r_p)}{r_p} = \frac{\Gamma(1/2)\Gamma[(\gamma - 1)/2]}{\Gamma(\gamma/2)} \left(\frac{r_0}{r_p}\right)^{\gamma}. \qquad (5)$$

We show our results for $w_p(r_p)$ in Figure 5, where the errors are estimated using the jackknife method. Tabulated values for w_p are listed in Table 3 for the all-fields case. We only use data points where the mean number of quasar-quasar pairs in the r_p-bin is more than 10, and we therefore restrict our fits to scales $4\ h^{-1}$ Mpc $\lesssim r_p \lesssim 150\ h^{-1}$ Mpc. The parameters of the best-fit power-law for the all-fields case is $r_0 = 16.1 \pm 1.7\ h^{-1}$ Mpc and $\gamma = 2.33 \pm 0.32$ when the negative data point at $r_p = 18.84\ h^{-1}$ Mpc is excluded. When this negative data point is included in the fit we get $r_0 = 13.6 \pm 1.8\ h^{-1}$ Mpc and an unusually large $\gamma = 3.52 \pm 0.87$, which is caused by the drag of the negative point on the fit.[16] Using good fields only yields $r_0 = 15.2 \pm 2.7\ h^{-1}$ Mpc and $\gamma = 2.05 \pm 0.28$, shown in the right

[16] For the good-fields case the projected correlation function is positive over the full range that we fit.

TABLE 3
PROJECTED CORRELATION FUNCTION $w_p(r_p)$

r_p (h^{-1} Mpc)	$DD_{\rm mean}$	$RR_{\rm mean}$	$DR_{\rm mean}$	w_p/r_p	w_p/r_p Error
1.189	0.0	114.3	19.8	...	...
1.679	0.9	258.3	39.6	154	162
2.371	4.5	478.5	91.8	236	195
3.350	9.9	913.2	160.8	78.1	51.5
4.732	20.7	1864.1	359.9	91.3	41.6
6.683	32.4	3786.5	684.3	15.7	7.81
9.441	62.9	7158.5	1314.0	10.6	4.45
13.34	130.0	14551.2	2659.1	3.06	2.85
18.84	227.3	28598.1	5162.4	−0.681	0.913
26.61	488.5	56940.7	10123.8	0.516	0.810
37.58	871.7	111284.0	19955.6	0.437	0.395
53.09	1762.2	218346.8	38910.9	0.0675	0.259
74.99	3394.4	422580.9	75630.1	0.0484	0.145
105.9	6751.7	811406.0	145785.5	0.0674	0.0592
149.6	12425.7	1535320.8	274851.9	0.0228	0.0292
211.3	22655.1	2849970.6	509877.9	−0.0183	0.00992

NOTES.—Results for all fields. $DD_{\rm mean}$, $DR_{\rm mean}$, and $RR_{\rm mean}$ are the mean numbers of quasar-quasar, random-random, and quasar-random pairs within each r_p bin for the 10 jackknife samples; $w_p(r_p)/r_p$ is the mean value calculated from the jackknife samples.

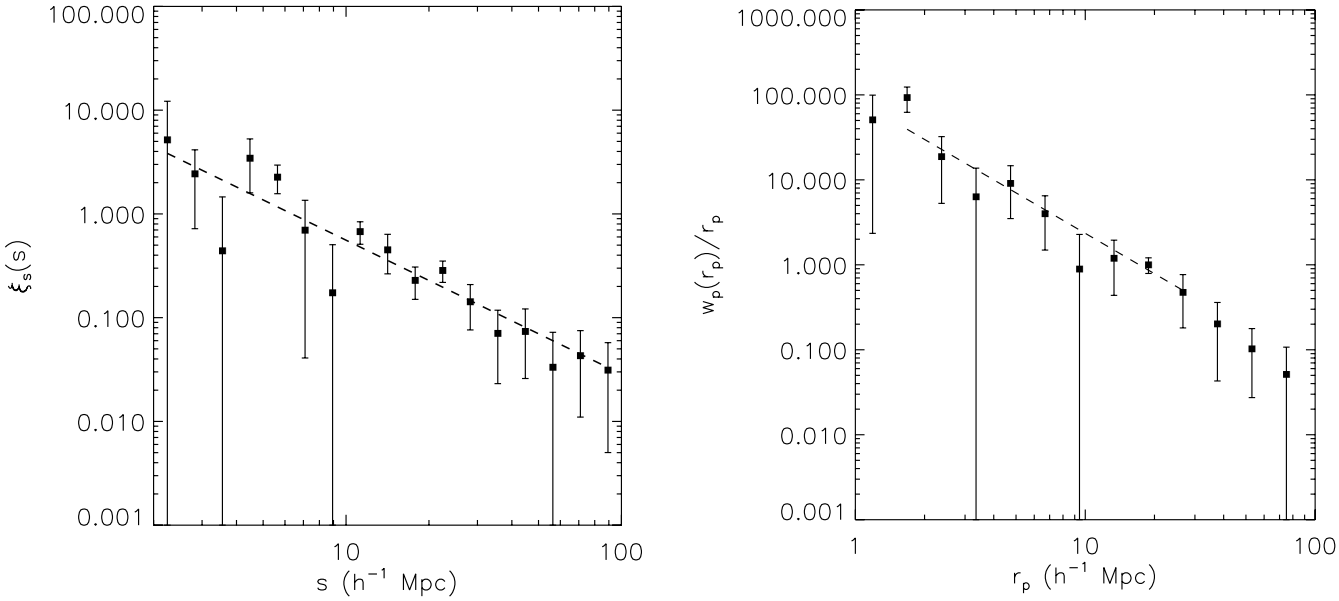

FIG. 6.—Correlation functions of 23,283 $0.8 \leq z \leq 2.1$ SDSS DR5 quasars in all fields. Errors are estimated using the jackknife method. *Left*: Redshift-space correlation function. *Right*: Projected correlation function. Also plotted are the best-fit power-law functions, with fitted parameters listed in Table 4.

panel of Figure 5. Note that the real-space correlation function indicates appreciably stronger clustering than does its counterpart in redshift space; the large redshift errors spread structures out in redshift space, diluting the clustering signal.

We have already indicated that the clustering signal is appreciably stronger than at lower redshift. To check that this was not somehow an artifact of our processing we selected a sample of 23,283 spectroscopically confirmed quasars with $0.8 \leq z \leq 2.1$ from the SDSS DR5, with the same selection criteria as we used above (§ 2.2). Figure 6 shows the resulting $\xi_s(s)$ and $w_p(r_p)$; to compare with the results of other authors (e.g., da Ângela et al. 2005; A. J. Connolly et al. 2007, in preparation), we integrated to $\pi_{\rm cutoff} = 70\ h^{-1}$ Mpc. We fit power laws over the range $1\ h^{-1}$ Mpc $< s < 100\ h^{-1}$ Mpc (Croom et al. 2005) for $\xi_s(s)$, and $1.2\ h^{-1}$ Mpc $< r_p < 30\ h^{-1}$ Mpc for $w_p(r_p)$ (PMN04 and da Ângela et al. 2005). The fitted power-law parameters are $s_0 = 6.36 \pm 0.89\ h^{-1}$ Mpc and $\delta = 1.29 \pm 0.14$ for $\xi_s(s)$, and $r_0 = 6.47 \pm 1.55\ h^{-1}$ Mpc and $\gamma = 1.58 \pm 0.20$ for $w_p(r_p)$. These results are in excellent agreement with Croom et al. (2005), PMN04, and da Ângela et al. (2005) based on the 2QZ sample, and A. J. Connolly et al. (2007, in preparation) based on the SDSS sample. Note that the 2QZ papers use a slightly different cosmology, which causes very little difference. More importantly, the 2QZ sample is at lower mean luminosity than the SDSS sample, although there is only a mild luminosity dependence of the clustering strength (e.g., Lidz et al. 2006; A. J. Connolly et al.

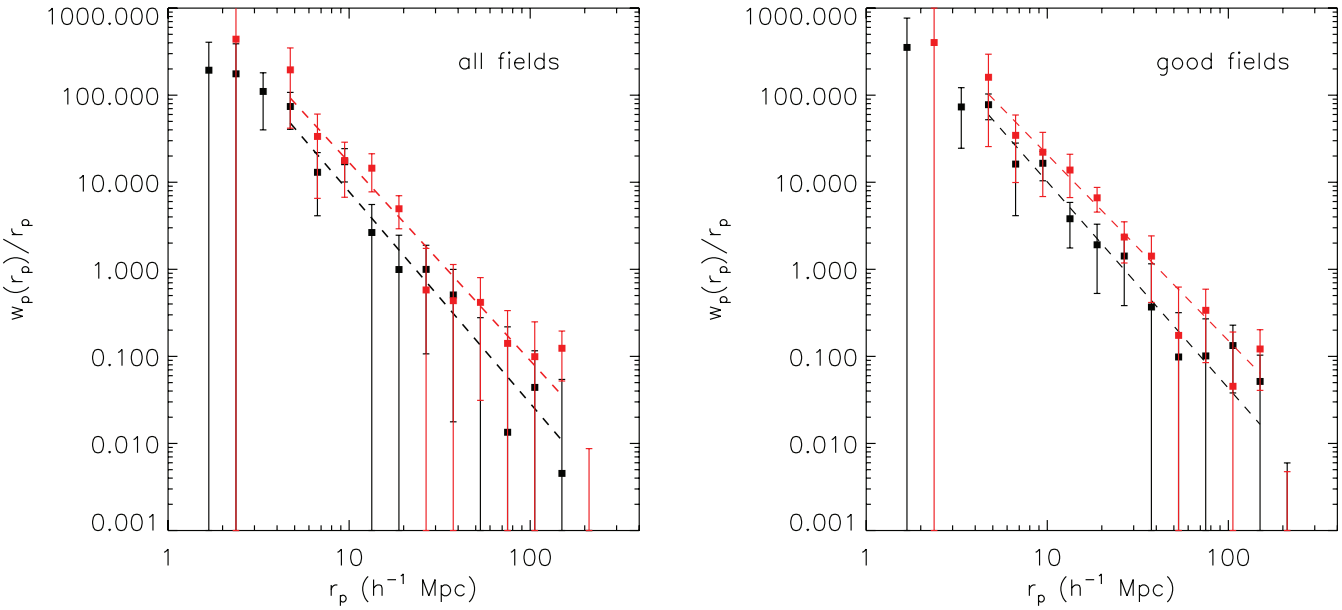

FIG. 7.—Clustering evolution of high-redshift quasars. Errors are estimated using the jackknife method. Black indicates the $2.9 \leq z \leq 3.5$ bin and red indicates the $z \geq 3.5$ bin. Also plotted are the best-fit power-law functions, with fitted parameters listed in Table 4. *Left*: All fields. *Right*: Good fields only. Both cases show stronger clustering in the higher redshift bin.

TABLE 4
SUMMARY OF THE FITTING PARAMETERS OF THE CORRELATION FUNCTION

Case	$\xi_s(s)/\xi(r)$	s_0/r_0 (h^{-1} Mpc)	δ/γ	χ^2/dof	s_0/r_0 (δ, $\gamma = 2.0$)	χ^2/dof
$z \geq 2.9$:						
All, Poisson	$(s/s_0)^{-\delta}$	10.16 ± 3.08	1.71 ± 0.43	0.47	...	...
All, jackknife	$(s/s_0)^{-\delta}$	10.39 ± 3.00	1.73 ± 0.46	0.37	...	...
All, jackknife[a]	$(s/s_0)^{-\delta}$	10.38 ± 2.57	2.07 ± 0.62	0.62	...	...
Good, Poisson	$(s/s_0)^{-\delta}$	12.72 ± 3.25	1.64 ± 0.31	0.35	...	...
Good, jackknife	$(s/s_0)^{-\delta}$	10.28 ± 2.95	1.43 ± 0.28	0.46	...	...
$z \geq 2.9$:						
All, jackknife	$(r/r_0)^{-\gamma}$	16.10 ± 1.70	2.33 ± 0.32	0.32	14.71 ± 1.86	0.42
All, jackknife[a]	$(r/r_0)^{-\gamma}$	13.60 ± 1.83	3.52 ± 0.87	0.75	...	...
Good, jackknife	$(r/r_0)^{-\gamma}$	15.16 ± 2.75	2.05 ± 0.28	0.75	14.81 ± 1.94	0.68
$2.9 \leq z \leq 3.5$:						
All, jackknife	$(r/r_0)^{-\gamma}$	16.02 ± 1.81	2.43 ± 0.43	0.43	14.79 ± 2.12	0.52
Good, jackknife	$(r/r_0)^{-\gamma}$	17.91 ± 1.51	2.37 ± 0.29	0.46	16.90 ± 1.73	0.56
$z \geq 3.5$:						
All, jackknife	$(r/r_0)^{-\gamma}$	22.51 ± 2.53	2.28 ± 0.31	0.50	20.68 ± 2.52	0.52
Good, jackknife	$(r/r_0)^{-\gamma}$	25.22 ± 2.50	2.14 ± 0.24	0.32	24.30 ± 2.36	0.32
$0.8 \leq z \leq 2.1$:						
All, jackknife	$(s/s_0)^{-\delta}$	6.36 ± 0.89	1.29 ± 0.14	0.88	...	...
	$(r/r_0)^{-\gamma}$	6.47 ± 1.55	1.58 ± 0.20	0.88	...	...

NOTES.—Fitting results for various cases and different redshift bins. The "Case" column indicates whether the correlation function is measured from all fields or from good fields only; it also indicates the error estimator. Here $\xi_s(s)$ is the redshift-space correlation function, while $\xi(r)$ is the real-space correlation function. The last two columns give the correlation length and reduced χ^2 for the fixed power-law index fits for selected cases.

[a] Data points with negative correlation function are included in the fit.

2007, in preparation). We note that the amplitude of $w_p(r_p)$ for $r_p \gtrsim 30\ h^{-1}$ Mpc is lower than predicted from the power-law fit, which is also the case in da Ângela et al. (2005, Fig. 2).

The predicted correlation function of the underlying dark matter at $r = 15\ h^{-1}$ Mpc is $\sim$0.014 at $z = 3.5$ (see § 3.3 and Appendix C), far below that of the current high-redshift quasar sample (Fig. 5), indicating that our high-redshift quasar sample is very strongly biased.

The increase in clustering signal with redshift we have seen suggests that we may be able to see redshift evolution *within* our sample. We divide our clustering sample into two subsamples with redshift intervals $2.9 \leq z \leq 3.5$ and $z \geq 3.5$. The resulting $w_p(r_p)$ are shown in Figure 7. The higher redshift bin shows systematically stronger clustering than does the lower redshift bin. The fitted parameters are $r_0 = 16.0 \pm 1.8\ h^{-1}$ Mpc and $\gamma = 2.43 \pm 0.43$ for $2.9 \leq z \leq 3.5$, and $r_0 = 22.5 \pm 2.5\ h^{-1}$ Mpc and $\gamma = 2.28 \pm 0.31$ for $z \geq 3.5$, where the fitting range is $\sim$4–150 h^{-1} Mpc. Using good fields only yields $r_0 = 17.9 \pm 1.5\ h^{-1}$ Mpc and $\gamma = 2.37 \pm 0.29$ for $2.9 \leq z \leq 3.5$, and $r_0 = 25.2 \pm 2.5\ h^{-1}$ Mpc and $\gamma = 2.14 \pm 0.24$ for $z \geq 3.5$. When we fix the power-law index to be $\gamma = 2.0$ we get slightly different but consistent correlation lengths for each case (Table 4). Indeed, the clustering of quasars increases strongly with redshift over the range probed by our sample.

The increase in clustering strength with redshift may be due to two effects: an ever-increasing bias of the halos hosting quasars with fixed luminosity with redshift, and luminosity-dependent clustering. The higher redshift quasars are more luminous (Table 6 and Fig. 17 of Richards et al. 2006) and may be associated with more massive halos. At low redshift ($z \lesssim 3$) and moderate luminosities, luminosity depends on accretion rate as much as black hole mass, and one expects little dependence of clustering strength on luminosity (Lidz et al. 2006), as observed (Croom et al. 2005; A. J. Connolly et al. 2007, in preparation). However, the high-luminosity, high-redshift quasars in our sample have close to Eddington luminosities (Kollmeier et al. 2006), and therefore we may well expect a strong dependence of the clustering signal on luminosity (Hopkins et al. 2006). We are limited by the relatively small size of our sample to date, and will explore the dependence of clustering strength with luminosity in a future paper.

Figure 8 shows the evolution of comoving correlation length r_0 as a function of redshift, where the data points for low-redshift bins (*gray triangles*) are taken from Porciani & Norberg (2006; the 2QZ sample). Data points for the SDSS quasar sample in this paper are denoted as filled squares, placed at the mean redshifts for each redshift bin. The black square is for the $0.8 \leq z \leq 2.1$ SDSS quasars, taken from the variable power-law index fit; the red and green squares are for the $2.9 \leq z \leq 3.5$ bin and the $z \geq 3.5$ bin (with γ fixed to 2.0), both for the all-fields case and the good-fields case. There are many factors that affect the fitted value of r_0: the 2QZ and the SDSS samples probe different

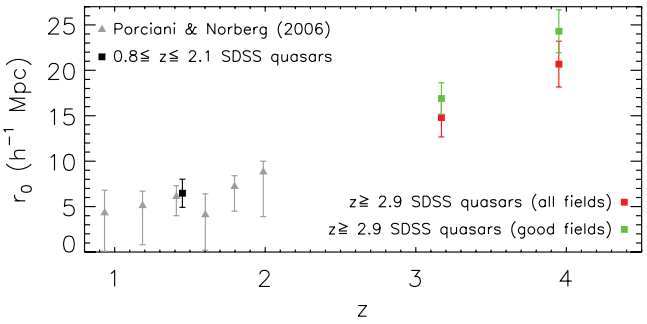

FIG. 8.—Evolution of the comoving correlation length r_0 as a function of redshift. Gray triangles are 2QZ data points taken from Porciani & Norberg (2006, col. [7] in their Table 3). The black square is for the $0.8 \leq z \leq 2.1$ SDSS quasars, taken from the variable power-law index fit; the red and green squares are for the $2.9 \leq z \leq 3.5$ and $z \geq 3.5$ bins for the all-fields and good-fields cases, respectively, taken from the fixed $\gamma = 2.0$ fits.

luminosities, the range of scales over which the power law is fit are different, and the power-law indices γ are different. Nevertheless, this figure demonstrates that the clustering length of quasars increases dramatically with redshift.

3.3. *Quasar Lifetime, Halo Mass, and Bias*

The clustering of quasars and their space density can be used to constrain the average quasar lifetime t_Q and the bias of the dark matter halos in which they sit (Martini & Weinberg 2001; Haiman & Hui 2001).[17] In this section, we follow Martini & Weinberg (2001); the essential formulae are presented in Appendix C. The basic assumptions are that (1) luminous quasars only reside in dark matter halos with mass above some threshold mass $M_{\rm min}$, and (2) those dark matter halos with $M \geq M_{\rm min}$ host at most one active quasar at a time. The probability that such a halo harbors an active quasar is the duty cycle t_Q/t_H, where t_H is the halo lifetime, given by equation (C6). Assumptions 1 and 2 include the assumption that every dark matter halo harbors a supermassive black hole, either active or dormant, and that the resulting quasars have the same clustering strength as their hosting halos.

We note that the Martini & Weinberg approach is appropriate for high-redshift quasars because at low redshift ($z < 2$), the occurrence of quasar activity is determined by fueling as well, rather than by the mere existence of a dark matter halo. Therefore the probability that a halo harbors an active quasar is the duty cycle t_Q/t_H times the (unknown) probability that a halo harbors an active or dead quasar.

The value of $M_{\rm min}(z)$ is related to the quasar lifetime and the observed quasar spatial density $\Phi(z)$ integrated over the survey magnitude range (having corrected for the selection function, of course):

$$\Phi(z) = \int_{M_{\rm min}}^{\infty} dM \, \frac{t_Q}{t_H(M,\ z)} n(M,\ z), \tag{6}$$

where we set the duty cycle t_Q/t_H equal to unity in the integration when $t_Q > t_H$, and $n(M,\ z)$ is the dark matter halo mass function. Here we follow Sheth & Tormen (1999) to compute $n(M,\ z)$. Given $\Phi(z)$ and assumed constant t_Q, we can determine $M_{\rm min}(z)$ from equation (6) and hence the effective bias $b_{\rm eff}(M_{\rm min},\ z)$ from equation (C8), for which we have used the analytical bias formalism in Jing (1998). We have checked the accuracy of the analytical bias model using the results of a cosmological N-body simulation by P. Bode and J. P. Ostriker (P. Bode 2006, private communication). At the simulation output redshifts, $z = 3$ and $z = 4$, the bias factor depends on scale. However, we will integrate over a range of scales (see eq. [7] below); the scale-independent analytical bias formalism provides an adequate prescription (see further discussion in Appendix C). More importantly, the analytic form allows us to interpolate the bias with redshift, which is needed to predict the observed correlation function (eq. [C11]). Figure 9 shows $n(M,\ z)$, $t_H(M,\ z)$, and $b_{\rm eff}(M,\ z)$ as functions of halo mass M (in units of $h^{-1}\ M_\odot$) at redshift $z = 3, 3.5$, and 4 for our standard cosmology.

We compute the model-predicted quasar correlation function $\xi_{\rm model}(r,\ z) = b_{\rm eff}^2 \xi_m(r,\ z)$ in steps of 0.1 in redshift, and integrate it to obtain the averaged correlation function $\bar{\xi}(r)$ over some redshift range via equation (C11). The function $\bar{\xi}(r)$ is to be compared with our measured correlation function $\xi(r)$. We iterate until we find a proper t_Q to minimize the difference between $\xi(r)$ and $\bar{\xi}(r)$. In practice, to compare the data and the model, we use the *integrated correlation function* within $[r_{\rm min},\ r_{\rm max}]\ h^{-1}$ Mpc, defined as

$$\xi_{20} = \frac{3}{r_{\rm max}^3} \int_{r_{\rm min}}^{r_{\rm max}} \xi(r) r^2 dr, \tag{7}$$

where we choose $r_{\rm min} = 5\ h^{-1}$ Mpc to minimize nonlinear effects and $r_{\rm max} = 20\ h^{-1}$ Mpc to maximize signal-to-noise ratio; within this range of scales, the model-predicted and measured correlation functions are well approximated by a single power law. If we assume $\xi(r) = (r/r_0)^{-\gamma}$, equation (7) reduces to

$$\xi_{20} = \frac{3 r_0^\gamma}{(3-\gamma) r_{\rm max}^3} \left(r_{\rm max}^{3-\gamma} - r_{\rm min}^{3-\gamma} \right). \tag{8}$$

Because the underlying dark matter correlation function within this scale range has a power-law index close to 2.0, we adopt values from the fixed $\gamma = 2.0$ fitting results in Table 4 instead of the variable power-law index fitting results. Hence we have $\xi_{20} = 1.230 \pm 0.353$ for the $2.9 \leq z \leq 3.5$ bin and $\xi_{20} = 2.406 \pm 0.586$ for the $z \geq 3.5$ bin, here using the results from all fields.

Our adopted values of $\Phi(z)$ are taken from the maximum-likelihood fitted quasar luminosity function with variable power-law index given by Richards et al. (2006), integrated from the

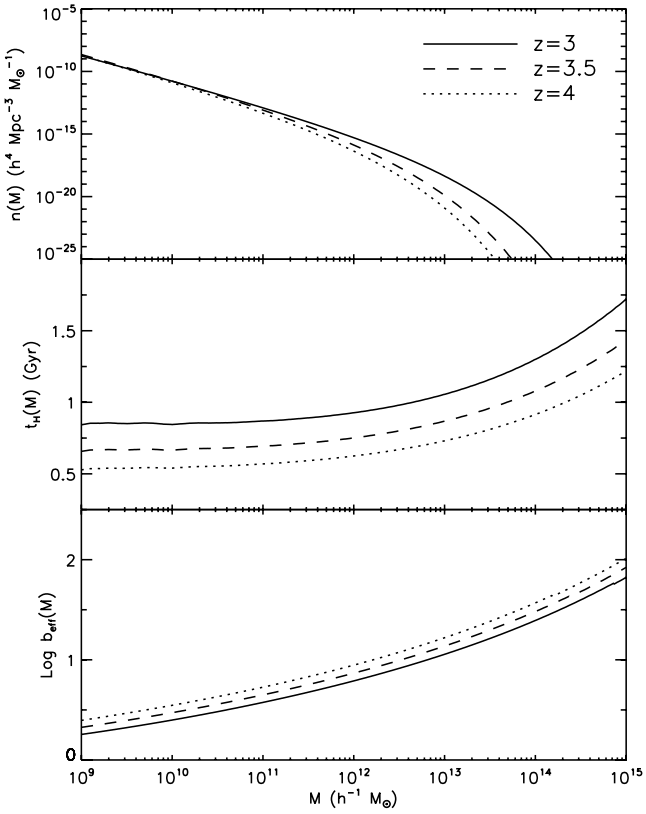

FIG. 9.—Sheth & Tormen (1999) halo mass function, halo lifetime, and effective bias factors for halos with $M > M_{\rm min}$ as functions of halo mass for three redshifts $z = 3,\ 3.5,\ 4$ in our fiducial cosmology. The age of the universe at these three redshifts is 2.2, 1.9, and 1.6 Gyr, respectively, and for typical halos with a mass of a few $\times\ 10^{12}\ h^{-1}\ M_\odot$, the halo lifetime is approximately $0.7 \sim 1$ Gyr at these redshifts.

[17] Here we define t_Q to be the total time that an accreting supermassive black hole has a UV luminosity above the luminosity threshold of our sample. If the black hole is as old as its host dark matter halo, then the duty cycle t_Q/t_H is the probability that we observe a quasar in this halo. Indeed, while the equations in Appendix C show that the directly constrained quantity is the duty cycle, the quantity t_Q indicates how much time a supermassive black hole spends during the luminous accretion phase as it assembles most of its mass.

TABLE 5

TRIAL VALUES OF t_Q AT REDSHIFT $z = 3.0,\ 3.5,\ 4.0$ AND THE CORRESPONDING $M_{\rm min}$ AND $b_{\rm eff}$, ASSUMING THE FIDUCIAL ΛCDM COSMOLOGY

z	Φ (h^3 Mpc^{-3})	t_Q (Gyr)	$M_{\rm min}$ ($h^{-1}\ M_\odot$)	$b_{\rm eff}$
3.0.....	5.591×10^{-7}	0.01	2.33×10^{12}	7.6
		0.1	6.10×10^{12}	9.8
		1	1.32×10^{13}	12.3
3.5.....	3.251×10^{-7}	0.01	2.09×10^{12}	9.0
		0.1	4.98×10^{12}	11.4
		1	9.76×10^{12}	13.9
4.0.....	1.009×10^{-7}	0.01	2.29×10^{12}	11.1
		0.1	4.87×10^{12}	13.7
		1	8.41×10^{12}	16.0

faintest i-band magnitude $i = 20.2$. That paper uses a slightly different cosmology from our own; we correct by the ratio of comoving volume elements. Figure 20 of Richards et al. (2006) shows that the functional fit we are using here does not perfectly follow the data, giving values of $\Phi(z)$ as much as a factor of 1.5 off from the actual value; in particular, the variable power-law fit function in Richards et al. (2006) appears to underestimate the value of $\Phi(z)$ at $z < 4.5$ but overestimate the value at $z > 4.5$ a little bit. This will probably cause slight underestimation and

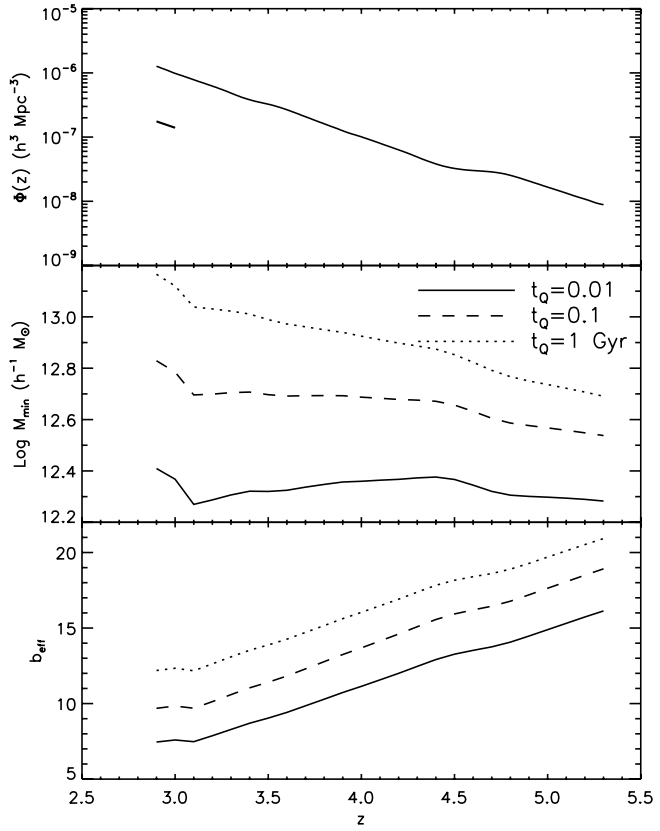

FIG. 10.—*Top*: Integrated quasar luminosity function down to the magnitude cut $i = 20.2$, computed using the variable power-law fit function in Richards et al. (2006). The lower line segment shows the integrated luminosity function down to $i = 19.1$. *Middle and bottom*: Computed minimum halo masses and effective bias factors as functions of redshift for the three trial values of $t_Q = 0.01,\ 0.1$, and 1 Gyr. We have used the empirical values of Φ at the grid points $z = 2.9$ and 3.0 (i.e., 3 and 4 times the values down to $i = 19.1$, respectively), which causes the jump in $M_{\rm min}$ and $b_{\rm eff}$ at these two redshift grid points; i.e., we are targeting more luminous quasars at $z = 2.9,\ 3.0$. The slight kink around $z = 4.5$ in all three panels is due to the K-correction (see Fig. 17 of Richards et al. 2006).

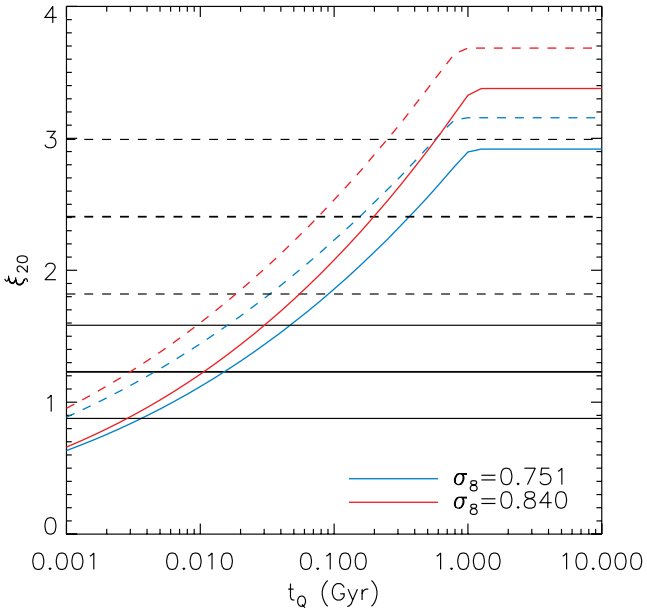

FIG. 11.—Comparison of the measured and model-predicted clustering strength ξ_{20}, defined in eq. (7). Solid lines correspond to the $2.9 \le z \le 3.5$ bin, and dashed lines correspond to the $z \ge 3.5$ bin. The thick and light horizontal lines show the measured clustering strength and 1 σ errors. The match of the model-predicted ξ_{20} (blue lines for the fiducial $\sigma_8 = 0.751$ and red lines for $\sigma_8 = 0.84$) with the measured ξ_{20} gives the average quasar lifetime t_Q within that redshift bin. The uncertainty in measured ξ_{20} gives a large uncertainty in t_Q. Quasars in the higher redshift bin have larger t_Q on average. The fiducial values of t_Q inferred from this figure (the $\sigma_8 = 0.751$ case) are $t_Q = 15$ Myr for $2.9 \le z \le 3.5$ and $t_Q = 160$ Myr for $z \ge 3.5$.

overestimation of t_Q (eq. [6]) for the lower and higher redshift bins, respectively, but the effect is tiny compared with other uncertainties. Table 6 lists the values of $\Phi(z)$ we have calculated, along with other quantities. The limiting absolute i-band magnitude at each redshift is calculated using the same cosmology and K-correction as in Richards et al. (2006), normalized to $z = 2$. One subtlety is that quasars at $z \le 3.0$ are close to the color cut at which the magnitude limit of the quasar sample changes between $i = 19.1$ and 20.2 (see Fig. 17 of Richards et al. 2006). To account for this effect, we use 3 times the density down to $i = 19.1$ for the redshift grid point at $z = 2.9$ and 4 times the density down to $i = 19.1$ for the redshift grid point at $z = 3.0$; the grid points with $z \ge 3.1$ use the integrated luminosity function to $i = 20.2$ (see Fig. 17 of Richards et al. 2006). In practice, our results are insensitive to these details.

To illustrate the relationship between t_Q, $b_{\rm eff}$, and $M_{\rm min}$, we choose fixed values of $t_Q = 0.01,\ 0.1,\ 1$ Gyr at each redshift and obtain the corresponding $M_{\rm min}$ and $b_{\rm eff}$ at $z = 3.0$, 3.5, and 4.0, listed in Table 5. Figure 10 shows the evolution of the integrated quasar number density $\Phi(z)$, $M_{\rm min}(z)$, and $b_{\rm eff}(z)$ for the three trial values of t_Q. At each redshift we obtain the model-predicted correlation function $\xi_{\rm model}(r,\ z)$, which is then averaged over our sample redshift range weighted by the observed quasar distribution (not corrected for the selection function) following equation (C11).

We compare the model predictions and measured values for the $2.9 \le z \le 3.5$ and $z \ge 3.5$ redshift bins, respectively. Figure 11 plots the model-predicted ξ_{20} as a function of t_Q for the two redshift bins. Above $t_Q \sim 1$ Gyr, the duty cycle saturates at unity, and the predicted correlation function flattens. The horizontal lines show the values and 1 σ errors of ξ_{20} computed using our fixed power-law fits, for the two redshift bins. For the $2.9 \le z \le 3.5$ bin,

TABLE 6
QUASAR SPACE DENSITY, $M_{\rm min}$, AND $b_{\rm eff}$ AT EACH REDSHIFT GRID

z	$M_{i,\,\rm limit}$ ($z = 2$)	$\Phi'(M_i < M_{i,\,\rm limit})$ (h^3 Mpc^{-3})	Φ (h^3 Mpc^{-3})	$n_{\rm QSO}$ (h^3 Mpc^{-3})	$D(z)$	$M_{\rm min}$ ($h^{-1}\,M_\odot$)	$b_{\rm eff}$
2.9.....	...	4.533×10^{-7}	5.268×10^{-7}	1.820×10^{-7}	0.3375	3.11×10^{12}	7.8
2.9*	−26.42	1.092×10^{-6}	1.268×10^{-6}	...	...	...	...
2.9**	−27.52	1.511×10^{-7}	1.756×10^{-7}	...	...	...	...
3.0.....	...	4.808×10^{-7}	5.592×10^{-7}	2.642×10^{-7}	0.3293	2.81×10^{12}	8.0
3.0*	−26.51	8.445×10^{-7}	9.821×10^{-7}	...	...	...	...
3.0**	−27.61	1.202×10^{-7}	1.398×10^{-7}	...	...	...	...
3.1.....	−26.59	6.722×10^{-7}	7.826×10^{-7}	2.735×10^{-7}	0.3214	2.26×10^{12}	7.9
3.2.....	−26.66	5.345×10^{-7}	6.228×10^{-7}	3.102×10^{-7}	0.3139	2.33×10^{12}	8.3
3.3.....	−26.74	4.156×10^{-7}	4.847×10^{-7}	2.369×10^{-7}	0.3068	2.43×10^{12}	8.7
3.4.....	−26.82	3.272×10^{-7}	3.820×10^{-7}	1.551×10^{-7}	0.3000	2.49×10^{12}	9.1
3.5.....	−26.84	2.783×10^{-7}	3.251×10^{-7}	1.254×10^{-7}	0.2934	2.48×10^{12}	9.4
	−26.84	2.783×10^{-7}	3.251×10^{-7}	1.254×10^{-7}	0.2934	5.76×10^{12}	11.9
3.6.....	−26.88	2.283×10^{-7}	2.670×10^{-7}	1.406×10^{-7}	0.2871	5.66×10^{12}	12.3
3.7.....	−26.96	1.774×10^{-7}	2.076×10^{-7}	1.462×10^{-7}	0.2811	5.66×10^{12}	12.8
3.8.....	−27.04	1.377×10^{-7}	1.612×10^{-7}	1.453×10^{-7}	0.2753	5.64×10^{12}	13.3
3.9.....	−27.12	1.070×10^{-7}	1.254×10^{-7}	9.720×10^{-8}	0.2698	5.62×10^{12}	13.7
4.0.....	−27.17	8.608×10^{-8}	1.009×10^{-7}	7.656×10^{-8}	0.2644	5.53×10^{12}	14.2
4.1.....	−27.24	6.821×10^{-8}	8.002×10^{-8}	6.413×10^{-8}	0.2593	5.46×10^{12}	14.7
4.2.....	−27.32	5.389×10^{-8}	6.326×10^{-8}	5.147×10^{-8}	0.2544	5.39×10^{12}	15.1
4.3.....	−27.41	4.171×10^{-8}	4.898×10^{-8}	4.322×10^{-8}	0.2496	5.34×10^{12}	15.6
4.4.....	−27.49	3.253×10^{-8}	3.823×10^{-8}	2.950×10^{-8}	0.2450	5.28×10^{12}	16.1
4.5.....	−27.53	2.763×10^{-8}	3.248×10^{-8}	3.040×10^{-8}	0.2406	5.10×10^{12}	16.5
4.6.....	−27.50	2.566×10^{-8}	3.018×10^{-8}	2.590×10^{-8}	0.2364	4.81×10^{12}	16.7
4.7.....	−27.45	2.437×10^{-8}	2.867×10^{-8}	2.435×10^{-8}	0.2323	4.51×10^{12}	17.0
4.8.....	−27.46	2.154×10^{-8}	2.535×10^{-8}	1.846×10^{-8}	0.2283	4.31×10^{12}	17.3
4.9.....	−27.54	1.754×10^{-8}	2.066×10^{-8}	1.492×10^{-8}	0.2245	4.21×10^{12}	17.7
5.0.....	−27.64	1.411×10^{-8}	1.662×10^{-8}	7.542×10^{-9}	0.2207	4.12×10^{12}	18.2
5.1.....	−27.74	1.136×10^{-8}	1.339×10^{-8}	3.177×10^{-9}	0.2171	4.03×10^{12}	18.6
5.2.....	−27.85	9.163×10^{-9}	1.080×10^{-8}	3.853×10^{-9}	0.2137	3.93×10^{12}	19.1
5.3.....	−27.95	7.502×10^{-9}	8.847×10^{-9}	3.895×10^{-9}	0.2103	3.83×10^{12}	19.5

NOTES.—$M_{i,\,\rm limit}$ is the i-band limiting absolute magnitude, K-corrected to $z = 2$; Φ' is the integrated quasar number density over the apparent magnitude range, in the same cosmology as in Richards et al. (2006), converted using $h = 0.7$ to units of h^3 Mpc^{-3}; Φ is the corresponding quasar number density in our cosmology, converted using $h = 0.71$ to h^3 Mpc^{-3}. There are three entries for each of the $z = 2.9$ and $z = 3.0$ grids, corresponding to magnitude limits of $i = 20.2$ (one asterisk) and $i = 19.1$ (two asterisks), and using the empirical values we adopted at these two redshift grids (see text; no asterisks). The apparent i-band limiting magnitude cut is $i = 20.2$ for $z \geq 3.1$. Here $n_{\rm QSO}$ is the observed overall quasar number density for all fields, in the current cosmology; the difference between $n_{\rm QSO}$ and Φ reflects the selection function and difference between the fitted power-law function and binned luminosity function. $D(z)$ is the linear growth factor. Also tabulated are the corresponding minimal halo mass $M_{\rm min}$ and effective bias factors $b_{\rm eff}$ at each redshift grid, computed using the fiducial values of t_Q, i.e., $t_Q = 15$ Myr for $2.9 \leq z \leq 3.5$ and $t_Q = 160$ Myr for $z \geq 3.5$.

the estimated quasar lifetime is $t_Q \sim 15$ Myr with lower limit 3.6 Myr and upper limit 47 Myr for the 1 σ error of the measured ξ_{20}. For the $z \geq 3.5$ redshift bin, the estimated quasar lifetime is $t_Q \sim 160$ Myr with lower limit ~30 Myr and upper limit ~600 Myr for the 1 σ error of the measured ξ_{20}. To phrase this in terms of the duty cycle, we take the average halo lifetime to be 1 Gyr at these redshifts (see Fig. 9). Therefore the duty cycle is ~0.004–0.05 for the lower redshift bin and ~0.03–0.6 for the higher redshift bin.

In the model we are using, t_Q is very sensitive to the clustering strength, as shown in Figure 11. A small change in the measured quasar correlation function will result in a substantial change in t_Q. Using different fitting results for the measured ξ_{20} (e.g., those for good fields only) will certainly change the value of t_Q. However, the formal 1 σ errors of t_Q are large enough to encompass these changes. The model is also sensitive to the adopted value of σ_8, whose consensus value has changed significantly since the release of the *WMAP* third-year data (Spergel et al. 2007). By increasing σ_8 we can increase the model-predicted ξ_{20} given the same t_Q.[18] The results for the *WMAP* first-year value $\sigma_8 = 0.84$ (Spergel et al. 2003) are also plotted in Figure 11 as red lines. In this case the t_Q values are slightly lower for the two redshift bins, but are still within the 1 σ errors of the fiducial σ_8 case. Combining these effects, we conclude that this approach can only constrain the quasar lifetime within a very broad range of 10^6–10^8 yr, which is, of course, consistent with many other approaches (e.g., Martini 2004 and references therein). On the other hand, our results do show, on average, a larger t_Q and duty cycle for the higher redshift bin.

There are other assumptions in our model that we should consider. In particular, there is the possibility that quasars cluster more than their dark matter halos due to physical effects that modulate the formation of quasars on very large scales. For example, the process of reionization may show large spatial modulation, which might affect the number density of young galaxies and quasars on large scales (e.g., Babich & Loeb 2006). We have also assumed that each halo hosts only one luminous quasar. However, Hennawi et al. (2006a) show that quasars (at lower redshift) are very strongly clustered on small scales, with some close binaries clearly in a single halo. Searches for multiple quasars at higher redshift have also been successful (J. Hennawi et al. 2007, in preparation), suggesting that at high-redshift as well, a single halo can host more than one quasar.

[18] The ξ_{20} result is insensitive to other cosmological parameters such as Ω_M.

Table 6 uses the fiducial values of t_Q we derived for the $\sigma = 0.751$ case to estimate the minimal halo mass and bias factors of high-redshift quasars, but the values of $M_{\rm min}$ and $b_{\rm eff}$ depend only weakly on t_Q, as one can see from Table 5. The values of $M_{\rm min}$ and $b_{\rm eff}$ are tabulated in Table 6, for each of the redshift bins. Note that the change of $M_{\rm min}$ within each redshift bin may not be real because we have assumed constant t_Q throughout the redshift bin. On the other hand, the host halos for the higher redshift bin have, on average, a larger minimal halo mass of $\sim(4-6)\times 10^{12}\ M_\odot$ than that for the lower redshift bin of $\sim(2-3)\times 10^{12}\ M_\odot$. This is expected, because quasars in the higher redshift bin have higher mean luminosity and hence should reside in more massive halos. From Table 6 it is clear that high-redshift quasars are strongly biased objects, and the effective bias factor increases with redshift.

4. SUMMARY AND CONCLUSIONS

We have used ∼4000 high-redshift SDSS quasars to measure the quasar correlation function at $z \geq 2.9$. The clustering of these high-redshift quasars is stronger than that of their low-redshift counterparts. Over the range of $4\ h^{-1}$ Mpc $< r_p <$ $150\ h^{-1}$ Mpc, the real-space correlation function is fitted by a power-law form $\xi(r) = (r/r_0)^{-\gamma}$ with $r_0 \sim 15\ h^{-1}$ Mpc and $\gamma \sim 2$. When we divide the clustering ample into two broad redshift bins, $2.9 \leq z \leq 3.5$ and $z \geq 3.5$, we find that the quasars in the higher redshift bin show substantially stronger clustering properties, with a comoving correlation length $r_0 = 24.3 \pm 2.4\ h^{-1}$ Mpc assuming a fixed power-law index $\gamma = 2.0$. The lower redshift bin has a comoving correlation length $r_0 = 16.9 \pm 1.7\ h^{-1}$ Mpc, assuming the same power-law index.

We followed Martini & Weinberg (2001) to relate this strong clustering signal to the quasar luminosity function (Richards et al. 2006), the quasar lifetime and duty cycle, and the mass function of massive halos. We find the minimum mass $M_{\rm min}$ of halos in which luminous quasars in our sample reside, as well as the clustering bias factor for these halos. High-redshift quasars are highly biased objects with respect to the underlying matter, while the minimal halo mass shows no strong evolution with redshift for our flux-limited sample. Quasars with $2.9 \leq z \leq 3.5$ reside in halos with typical mass $\sim(2-3)\times 10^{12}\ h^{-1}\ M_\odot$; quasars with $z \geq 3.5$ reside in halos with typical mass $\sim(4-6)\times 10^{12}\ h^{-1}\ M_\odot$. The slight difference of $M_{\rm min}$ in the two redshift bins is expected because quasars in the higher redshift bin have mean luminosity that is approximately two times that of quasars in the lower redshift bin, and should reside in more massive halos. We further estimated the quasar lifetime t_Q. We get a t_Q value of ∼4–50 Myr for the $2.9 \leq z \leq 3.5$ bin and ∼30–600 Myr for the $z \geq 3.5$ bin; which is broadly consistent with the quasar lifetime of 10^6–10^8 yr estimated from other methods (e.g., Martini 2004 and references therein). This corresponds to a duty cycle of ∼0.004–0.05 for the lower redshift bin and ∼0.03–0.6 for the higher redshift bin, where we take the average halo lifetime to be 1 Gyr. In general we find the average lifetime is higher for the higher redshift bin, which could either be due to the redshift evolution or an effect of the luminosity dependence of t_Q. However, we emphasize that our approach is subject to a variety of uncertainties, including errors in the clustering measurements themselves, uncertainties in σ_8 and the halo mass function, and the validity of the assumptions we have adopted.

It is interesting to note that recent *Chandra* and *XMM-Newton* studies on the clustering of X-ray selected AGNs have revealed a larger correlation length than optical AGNs. In particular, hard X-ray AGNs have a correlation length $r_0 \sim 15\ h^{-1}$ Mpc at $z \lesssim 2$ (e.g., Basilakos et al. 2004; Gilli et al. 2005; Puccetti et al. 2006; Plionis 2007). Given the fact that X-ray selected AGNs have considerably lower mean bolometric luminosity than do optically selected AGNs (e.g., Mushotzky 2004), this implies, once again, that the instantaneous luminosity is not a reliable indicator of the host halo mass at the low-luminosity end (e.g., Hopkins et al. 2005). Shen et al. (2007) have suggested an evolutionary model of AGN accretion in which an AGN evolves from being dominant in the optical to dominant in X-rays when the accretion rate drops. Hence those strongly clustering hard X-ray AGNs were probably once very luminous quasars in the past with high peak luminosities. When they dim and turn into hard X-ray sources, their spatial clustering strength remains. However, the current X-ray AGN sample is still very limited compared with optically selected samples, and hence the uncertainty in the X-ray AGN correlation length is large.

The work described in this paper can be extended in a variety of ways. Our sample cannot explore clustering below $\sim 1\ h^{-1}$ Mpc because of fiber collisions; we are extending the methods of Hennawi et al. (2006a) to find close pairs of high-redshift quasars, to determine whether the excess clustering found at moderate redshift extends to $z > 3$. Extending the clustering analysis to lower luminosities will be important, given theoretical predictions of a strong luminosity dependence to the clustering signal at high redshifts (Hopkins et al. 2006). The repeat scans of the southern equatorial stripe in SDSS (Adelman-McCarthy et al. 2007) will allow us to extend the luminosity range of our sample, and redshifts of the fainter quasars are already being obtained (Jiang et al. 2006). The massive halos that we predict host the luminous quasars must also contain a substantial number of ordinary galaxies, and we plan deep imaging surveys of high-redshift quasar fields to measure the quasar-galaxy cross-correlation function (see Stiavelli et al. 2005; Ajiki et al. 2006). Finally, more work is needed on simulations of quasar clustering. Our quasar lifetime/duty cycle calculation is frustratingly imprecise, and further explorations of the behavior of highly biased rare halos at high redshifts may yield ways to constrain duty cycles more directly from the data, and understand the uncertainties of the technique in more detail.

Finally, we need to make more detailed comparisons of high-redshift quasar clustering with that of luminous galaxies at the same redshift. The duty cycle of quasars at these redshifts is a few percent at most, and thus there is a population of galaxies with quiescent central black holes that is just as strongly clustered. The correlation length of Lyman break galaxies at these redshifts is $\sim 5\ h^{-1}$ Mpc (Adelberger et al. 2005b), but the clustering strength appears to increase (albeit at $z \sim 2$) with increasing observed K-band luminosity (Adelberger et al. 2005a; Allen et al. 2005) and/or color (Quadri et al. 2006). The duty cycle we have calculated should agree with the ratio of number densities of luminous quasars, and that of the parent host galaxy population. The challenge will be to identify this parent population unambiguously.

We thank Paul Bode and J. P. Ostriker for useful discussions and for providing us their numerical simulation results used in Appendix C, and Jim Gray for his work on the CAS. Y. S. and M. A. S. acknowledge the support of NSF grant AST 03-07409.

Funding for the SDSS and SDSS-II has been provided by the Alfred P. Sloan Foundation, the Participating Institutions, the National Science Foundation, the US Department of Energy, the National Aeronautics and Space Administration, the Japanese Monbukagakusho, the Max Planck Society, and the Higher Education Funding Council for England. The SDSS Web site is http://www.sdss.org.

The SDSS is managed by the Astrophysical Research Consortium for the Participating Institutions. The Participating Institutions are the American Museum of Natural History, Astrophysical Institute Potsdam, University of Basel, University of Cambridge, Case Western Reserve University, University of Chicago, Drexel University, Fermilab, the Institute for Advanced Study, the Japan Participation Group, Johns Hopkins University, the Joint Institute for Nuclear Astrophysics, the Kavli Institute for Particle Astrophysics and Cosmology, the Korean Scientist Group, the Chinese Academy of Sciences (LAMOST), Los Alamos National Laboratory, the Max Planck Institute for Astronomy (MPIA), the Max Planck Institute for Astrophysics (MPA), New Mexico State University, Ohio State University, University of Pittsburgh, University of Portsmouth, Princeton University, the United States Naval Observatory, and the University of Washington.

APPENDIX A

QUASAR REDSHIFT DETERMINATION

A1. BROAD EMISSION LINE SHIFTS

High-redshift quasars ($z \geq 2.9$) have only a few strong emission lines that fall within the SDSS spectral coverage (3800–9200 Å): Lyα (1216 Å), Si IV/O IV] (1397 Å), C IV (1549 Å), and C III] (1909 Å). The Lyα emission line is heavily affected by the Lyα forest and is blended with N V λ1240. In addition, high-ionization broad emission lines such as C IV are blueshifted by several hundred km s^{-1} from the redshift determined from narrow forbidden lines such as [O III] λ5007 (e.g., Gaskell 1982; Tytler & Fan 1992; Richards et al. 2002b). We could simply correct the redshift derived from each observed line for the (known) mean offset of that line from systemic (e.g., Vanden Berk et al. 2001; Richards et al. 2002b). We can do better than this, however, by examining the relationships between the shifts of different lines.

To understand these relationships, we use a sample of quasars drawn from the SDSS DR3 quasar catalog (Schneider et al. 2005) with $1.8 \leq z \leq 2.2$; for these objects, the lines Si IV, C IV, C III], and Mg II λ2800 all fall in the SDSS spectral coverage. The Mg II line has a small and known offset from the systemic redshift (Richards et al. 2002b), and thus tying our results to Mg II allows us to determine the systemic redshift for each object. We exclude from the sample those objects that show evidence for a broad absorption line, determined using the "balnicity" index (BI) of Weymann et al. (1991) and using the Vanden Berk et al. (2001) quasar composite spectrum to define the continuum level.

We fit a lognormal to each of the four lines (with a second lognormal added for the neighboring lines He II λ1640 and Al III λ1857), together with the local continuum. The centroid for each line is determined following Hennawi et al. (2006b): we calculate the mode of the pixels within $\pm 1.5\ \sigma$ of the fitted Gaussian line center using $3 \times \mathrm{median} - 2 \times \mathrm{mean}$. We include in the mode calculation those pixels with flux:

$$f_\lambda > \frac{0.6A_i}{\sqrt{2\pi}\sigma_i} + C_\lambda + \sum_{j \neq i} \frac{A_j}{\sqrt{2\pi}\sigma_j} e^{-(\log \lambda - \log \lambda_j)^2/2\sigma_j^2}, \quad \text{(A1)}$$

where A_i, $\log \lambda_i$, and σ_i are the amplitude, central wavelength, and dispersion of the best-fit lognormal to the ith emission line and C_λ is the linear continuum. Lines with a signal-to-noise ratio (S/N) less than 6 pixel^{-1}, or with lognormal fits with $\chi^2 > 5$, are rejected from further consideration. This gives us a sample of 1652 quasars with robust line measurements. Figure 12 shows the distribution of shifts between various lines. The means and standard deviations of these distributions are given in Table 7. The contribution from the line fitting error is negligible compared to the "intrinsic" dispersion of velocity shifts.

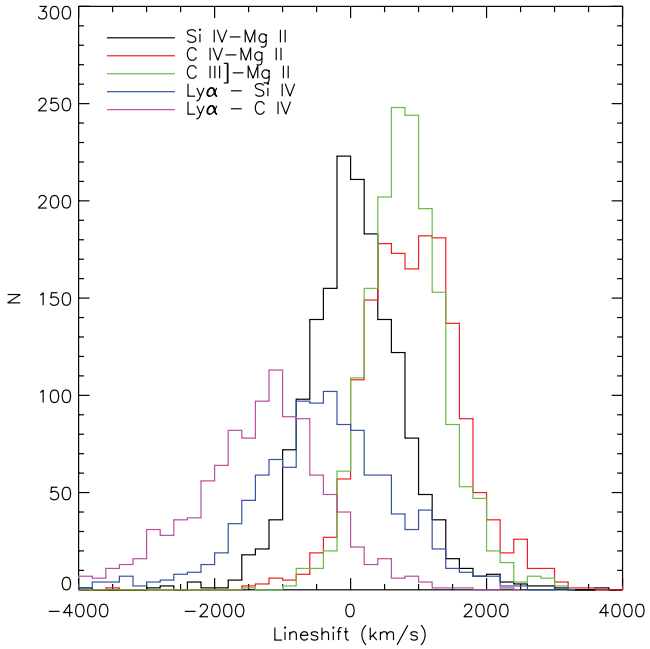

FIG. 12.—Distributions of relative shifts of the modes of various emission lines, as measured for 1652 high-S/N, non-BAL quasars with redshifts between 1.8 and 2.2. The mean values and 1 σ deviations of these line shifts are listed in Table 7.

These line shifts are correlated with each other, as Figure 13 shows. In each panel, we show the best-fit line to the correlations, giving each point equal weight. Given these correlations, we can use the shifts between the lines we observe at high redshift to determine the offset to Mg II, and thus to the systemic redshift.

There are also correlations between the line shifts and quantities such as the quasar luminosity, color, line width, and equivalent width. However, these correlations show large scatter and are therefore not as good for determining the true redshifts of the quasars.

A2. Lyα–Si IV, Lyα–C IV LINE SHIFTS

The C IV line lies beyond the SDSS spectra for $z > 4.9$. In addition, some quasars have weak metal emission lines, which are of too low S/N to allow us to measure a redshift from them. In these cases, we will measure the redshift from the Lyα line. In order to understand the biases that this gives, we selected a sample of 1114 non-BAL quasars with $2.9 < z < 4.8$ with high-S/N Si IV and C IV lines. The center of the Lyα line was taken to be the wavelength of maximum flux. To reduce the effects of fluctuations and strong skylines, we mask out 5 σ outliers from the 20 pixel smoothed spectrum and the 5577 Å skyline region (about 20 pixels), and smooth the spectrum by 15 pixels before identifying the peak pixel; all spectra were examined by eye to confirm that we correctly identified the peak of Lyα.

Figure 14 shows the shifts between Lyα and the C IV and Si IV lines as a function of redshift. The mean shift is $\sim$500 km s^{-1} with a 1 σ scatter of 1200 km s^{-1} for Lyα–Si IV, and $\sim$1500 km s^{-1} with a 1 σ scatter of 1200 km s^{-1} for Lyα–C IV. This systematic offset is caused by absorption blueward of the Lyα forest; over this redshift range, the increasing strength of the forest does not

TABLE 7
EMISSION-LINE SHIFTS

Parameter	Lyα–Si IV	Lyα–C IV	Si IV–Mg II	C IV–Mg II	C III]–Mg II	Mg II–[O III]
Mean velocity shift (km s^{-1})	−463	−1478	61	921	827	−97
σ (km s^{-1})	1178	1217	744	746	604	269

NOTES.—The Mg II–[O III] (i.e., systemic) line shift and 1 σ error are taken from Richards et al. (2002b). Positive values indicate a blueshift. The dispersion of the shift between C IV and Mg II is somewhat larger than the value of 511 km s^{-1} quoted by Richards et al. (2002b), but consistent with their recent result using a much larger sample from SDSS DR4 ($\sim$770 km s^{-1}).

cause an appreciable increase in the shift. The Lyα line is blended with the N V line; therefore whenever we use Lyα as the only estimator for redshift, we examine the spectrum by eye to confirm that we have identified the correct line.

A3. DETERMINATION OF REDSHIFTS

We are now ready to determine unbiased redshifts for our sample of $z \geq 2.9$ quasars. Given the first guess of the redshift of each object from Schneider et al. (2005) for those objects included in DR3, and from the two spectroscopic pipelines (§ 2.1), we fit the centroids of the Si IV, C IV, and C III] lines as we described above.

For objects in which the centroids of all three lines are well determined (we require that a line have a mean S/N per pixel >4 and reduced $\chi^2 < 10$), we base the redshift on the centroid of C IV. We measure the shift between C IV and Si IV, and the shift between C IV and C III], and determine from each the expected C IV–Mg II line shift using the correlations in Figure 13 and Table 8. We average these line shifts together and add on the small correction from Mg II to systemic given by Richards et al. (2002b); this gives our final C IV to systemic shift and hence the redshift. The uncertainty in these shifts gives rise to an uncertainty $\sigma_v = 519$ km s^{-1} or $\sigma_z = (1 + z)\sigma_v/c$.

For quasars with only two high-S/N lines, we take C IV whenever we have it and Si IV when C IV is absent (we avoid using C III] because it is often near the upper wavelength limit, 9200 Å, of the SDSS spectra). Again, we use the correlations of Figure 13 to compute the line shift relative to Mg II and therefore the shift

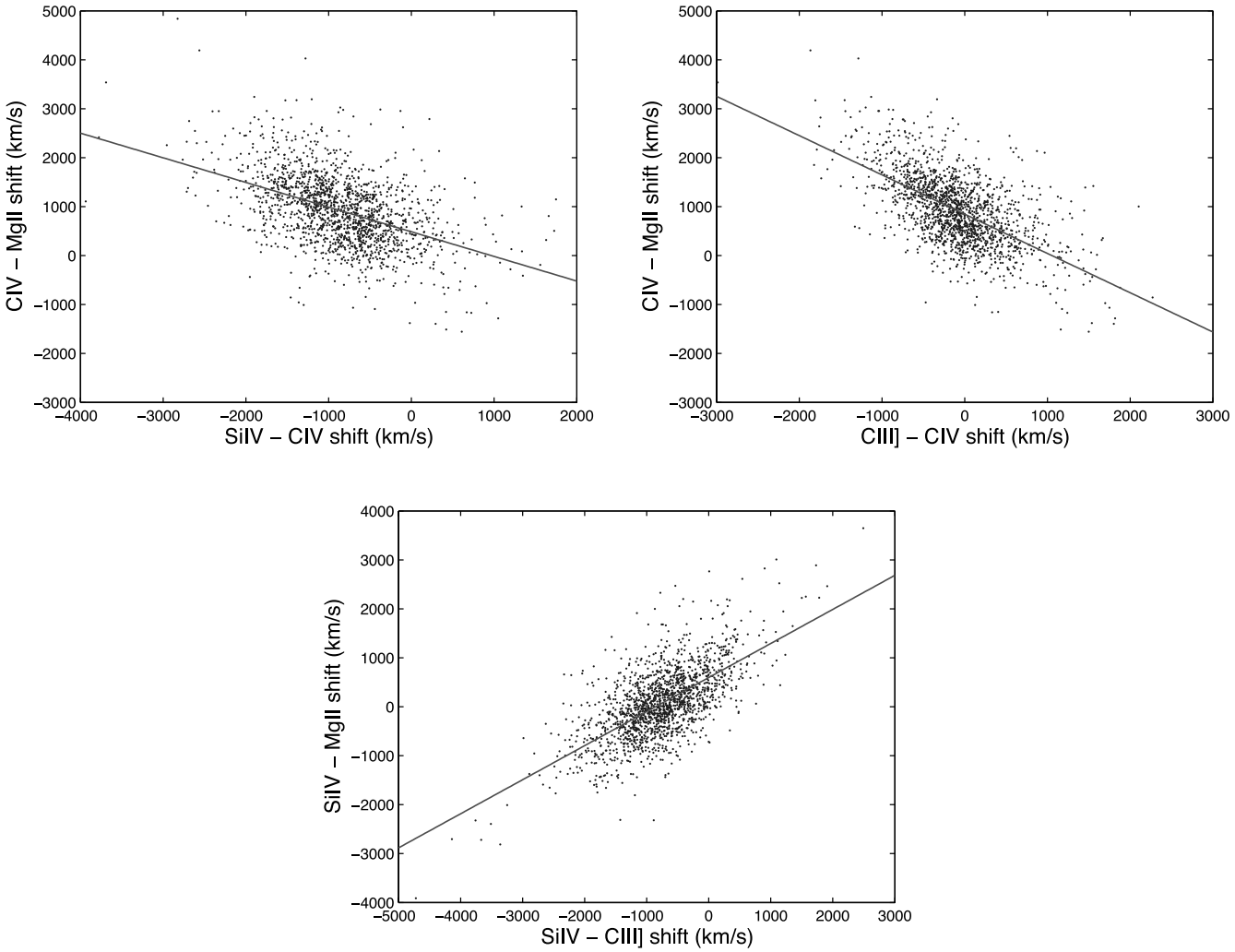

FIG. 13.—Correlations between various emission-line shifts. Dots are data points, and lines are fitted linear functions. These correlations are used in our redshift estimation. The fitted linear parameters and 1 σ deviations are listed in Table 8. [*See the electronic edition of the Journal for a color version of this figure.*]

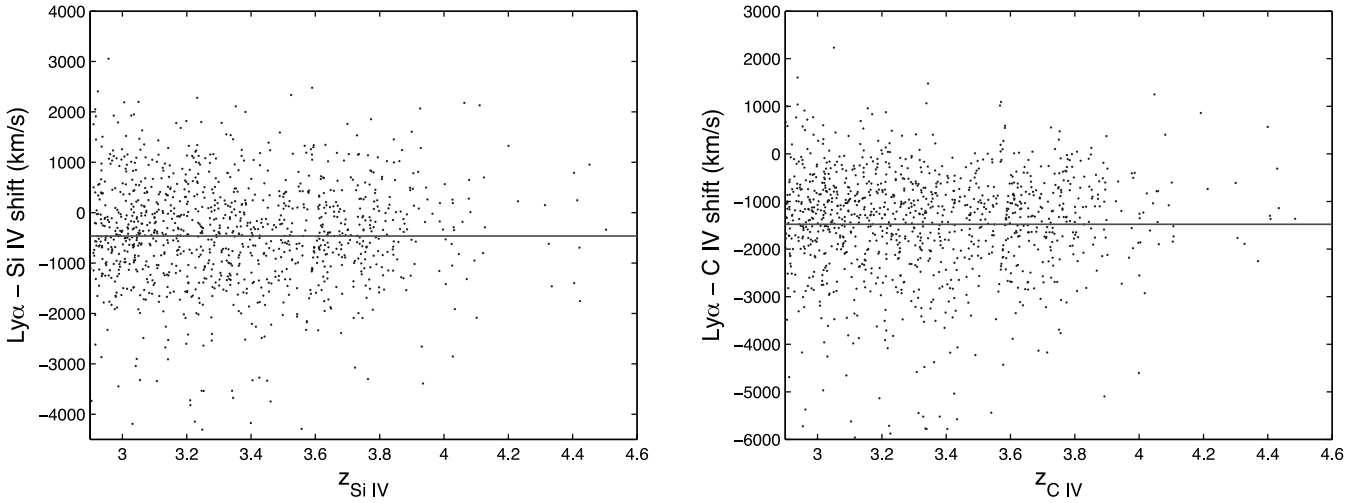

FIG. 14.—Relative shifts of Lyα vs. Si IV and C IV emission lines as a function of redshift. Lines indicate the mean values of line shifts. The mean values of line shifts and 1 σ deviations are listed in Table 7. [*See the electronic edition of the Journal for a color version of this figure.*]

relative to the systemic redshift. The velocity shift (relative to systemic) errors in this correction are 713 km s^{-1} if the two lines are Si IV and C IV, 629 km s^{-1} if the two lines are Si IV and C III], and 652 km s^{-1} if the two lines are C IV and C III]. For quasars with only one well-detected line, we use the average line shift, and use error transfer to determine the errors in the line shift relative to systemic. These errors are 791 km s^{-1} for Si IV, 793 km s^{-1} for C IV, and 661 km s^{-1} for C III]. Finally, for those quasars with no well-detected metal lines, we use Lyα to determine the redshift, using the average line shift relative to C IV and the corresponding 1 σ dispersion to compute the error: adding the uncertainties in the transformations in quadrature gives an error of 1453 km s^{-1}.

Finally, we examine the spectra of the following classes of objects by eye to check the redshift determinations: (1) the 407 objects with $|z_i - z_{\rm sys}| > 3\sigma_z$, where $z_{\rm i}$ is the initial redshift from the DR3 QSO catalog or SDSS spectroscopic pipeline; $z_{\rm sys}$ is our best estimation of redshift and σ_z is the estimated redshift error; (2) the 327 objects for which the redshift was based on Lyα; and (3) serendipitously found ambiguous cases. Of the $\sim$750 objects we inspected by eye, our redshift as determined above was superior to the value from Schneider et al. (2005) or the pipelines in 70% of the quasars; for 15%, at least one of the pipeline redshifts was correct and was therefore adopted, and for the remaining 15% (many of them are BAL), neither redshift was correct. In the latter case, we refit the redshift by hand and assigned a redshift error σ_z between 0.01 and 0.05, depending on how messy the spectrum was. There were 29 objects whose redshifts were undetermined, lay below 2.9, or were simply not quasars. Thus the parent sample, from which we will construct our clustering subsample, contains 6109 objects (including $\sim$200 duplicates).

Finally, we compared the redshifts in our sample with the separately compiled DR5 quasar sample of Schneider et al. (2006). The difference in redshifts follows a Gaussian distribution with zero mean and a dispersion of 0.01, comparable to our estimated errors.

TABLE 8
CORRELATIONS ($y = ax + b$)

Correlation	a	b (km s^{-1})	σ (km s^{-1})
C IV–Mg II vs. Si IV–C IV	−0.5035	486.7	660
C IV–Mg II vs. C III]–C IV	−0.8024	845.8	594
Si IV–Mg II vs. Si IV–C III]	0.6958	596.5	569

APPENDIX B

SURVEY GEOMETRY

SDSS spectroscopic targets are selected from the imaging data, and thus the spectroscopic footprint is a complicated combination of the individual runs which make up the imaging data, and the circular 1.49° radius tiles on which spectroscopic targets are assigned to fibers. Here we describe how this footprint is quantified. It will be useful in the following discussion to refer to Figure 15. Related discussions of the SDSS survey footprint in the context of galaxy samples may be found in Appendix A2 of Tegmark et al. (2004) and in Blanton et al. (2005).

As described in York et al. (2000), each imaging run of the SDSS covers part of a strip; two adjacent strips make a filled "stripe" of width 2.5°. Spectroscopic targeting to define a set of tiles is done off contiguous pieces of stripes termed "targeting chunks"; the SDSS imaging never got so far ahead of the spectroscopy as to allow a targeting chunk to work off more than one stripe at a time. The targeting in a given chunk all uses the same version of the target selection code (an important consideration for us, given the change in quasar target selection following DR1; § 2.2). Each targeting chunk is bounded on the east and west by lines of constant μ (i.e., the SDSS great circle coordinate; see Pier et al. 2003), and, for stripes in the northern Galactic cap, they are bounded in the north-south direction by lines of constant η (i.e., the SDSS survey coordinate) if in the northern stripes. Targeting chunks in the three stripes in the southern Galactic cap have no η boundary applied. Targeting chunks never overlap; therefore the union of targeting chunks defines the geometry of the targeting regions as a whole. Parameters defining the geometry of the targeting chunks can be found in a table called Chunk[19] in the CAS.

As described by Blanton et al. (2003), targets in each chunk are assigned to tiles, and then to fibers within each plate. We first define "tiling chunks" (referred to as "tiling regions" by Blanton et al. 2003, 2005), each of which is a set of non-overlapping tiling

[19] We used the TARGET (not BEST) version of the Chunk table.

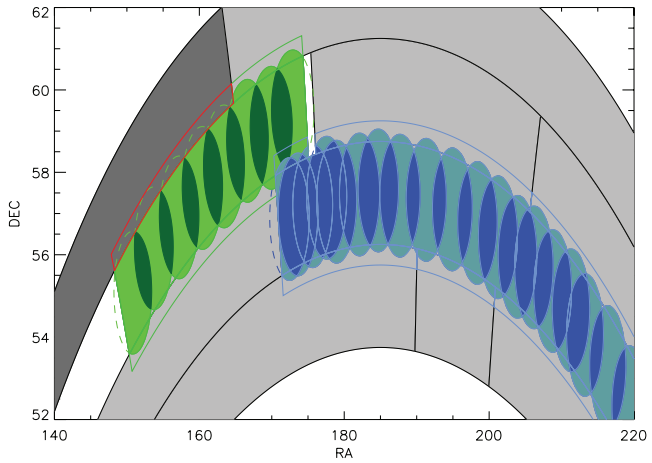

FIG. 15.—Portion of the targeting and tiling geometry in SDSS spectroscopy. The targeting chunks are denoted by stripes bounded by black lines, and each targeting chunk is targeted using one target version. Gray stripes are targeting chunks with target version no lower than v3_1_0 (not necessarily the same version); one dark gray targeting chunk shown here is targeted with target version v2_13_5. Within targeting chunks we carve out tiling rectangles, each of which is targeted with a unique version. A set of tiling rectangles form a tiling chunk. Shown here as examples are tiling chunk 38, which has one rectangle (*red*) targeted with version v2_13_5 and three rectangles (*green*) with version v3_1_0; and tiling chunk 67, whose rectangles (*blue*) are all with target version v3_1_0 or later. Within each tiling chunk we place tiles (1.49° radius circles, which appear as ellipses because the aspect ratio of the region of sky shown is not 1 : 1); tiles are trimmed by the boundaries of rectangles of that tiling chunk and balkanized (i.e., Hamilton & Tegmark 2004) into non-overlap sectors (which are covered by only one tile) and overlap sectors (which are covered by more than one tile). We use light and dark colors to denote the two types of sectors in the above two tiling chunks. Note that although balkanized sectors of the same tiling chunk do not intersect with each other, they could intersect with sectors of another tiling chunk. In the above case, the upper left corner rectangle in tiling chunk 67 is completely within the middle main rectangle of tiling chunk 38. Therefore, one should be careful when computing the effective area of sectors. In constructing our clean subsample for clustering analysis, we reject those sectors that are within tiling rectangles which are targeted with target version lower than v3_1_0, i.e., regions such as the red rectangle in chunk 38.

rectangles bounded by constant coordinates in different coordinate systems (all three types of coordinate systems, as well as the mixture of them are used in describing the tiling rectangles; and there is a flag indicating the coordinate type in the TilingBoundary table in the CAS). Each of these tiling rectangles lies completely within a single targeting chunk so that the target selection version is unique throughout the rectangle.

Although tiling rectangles of the same tiling chunk never overlap, tiling rectangles from different tiling chunks can overlap—for example, the upper left blue rectangle and the middle main green rectangle in Figure 15. On the other hand, a tiling rectangle never straddles two *targeting* chunks, so the target selection version is the same over the rectangle. A tiling chunk as a whole can straddle more than one targeting chunk and can have tiling rectangles that do not all use the same version of the target selection pipeline. A set of spectroscopic tiles of radius 1.49° are placed in each tiling chunk, and fibers assigned to the targeted objects therein, following the algorithm of Blanton et al. (2003). Thus because the tiles often extend beyond the boundaries of the tiling chunk (see Fig. 15), they do not include any targets beyond the tiling chunks. The intersection of the tiling rectangles and the circular tiles defines "sectors": each sector is covered by a unique set of tiles (see Fig. 3 of Blanton et al. 2005) and is a spherical polygon as described by Hamilton & Tegmark (2004). The union of all the sectors defines the angular coverage of the SDSS. We say a sector is a "non-overlap sector" if it is covered by only one tile (the lighter colors in Fig. 15) and is an "overlap sector" if it is covered by more than one tile (indicated with darker colors in the figure).

The tiling chunk geometry information is taken from the TilingBoundary table (which, itself, is a view of the TilingGeometry table with all the tiling masks removed) in the DR5 CAS server. We reject those tiling rectangles with target version lower than v3_1_0. The spectroscopic tile (plate) information is taken from the "maindr5spectro.par" table from the DR5 Web site,[20] which only includes tiles in the main survey and contains information of which tiling chunk each tile belongs to. We create the sectors by combining the two geometries using the spherical polygon description in Hamilton & Tegmark (2004). When computing the effective area of either all the non-overlap sectors or all the overlap sectors we use the *balkanization* procedure in A. Hamilton's product *mangle*[21] to reduce duplicate area.

After rejecting those tiling rectangles which used this earlier version, our sample covers a solid angle of 4041 deg^2, of which roughly 30% is in overlap sectors. Because quasars in the overlap regions are not subject to the restriction of not targeting pairs separated by less than 55″, and because the tiling algorithm deliberately places the tile overlap in regions of higher target density, one concern is that the angular selection function needs to take into account a higher selection function in the overlap region. However, we found that the number density of quasar candidates (here looking at all redshifts, not just the high-redshift candidates) and the number density of spectroscopically confirmed quasars were essentially identical in the overlap and non-overlap sectors. In contrast, the number density of spectroscopic galaxies in the overlap sectors (93.1 deg^{-2}) is 23% higher than that in the non-overlap sectors (75.4 deg^{-2}), due to the deliberate placing of the overlaps in regions of high target density; galaxies dominate the SDSS spectroscopic targets, and beyond a subtle effect due to gravitational lensing (Scranton et al. 2005), we expect no correlation between the background quasars and the foreground galaxies. All this means that the angular selection function of our sample can be assumed to be uniform within the mask defined by the sectors that make up our sample. For DR5, the overall spectroscopic completeness of quasar candidates is ∼95%, and the fraction of quasar candidates that are indeed quasars is ∼48%. The angular quasar number density is ∼9.4 deg^{-2}.

APPENDIX C

RELATIONSHIP BETWEEN HALO MASS, CLUSTERING STRENGTH, AND QUASAR LIFETIME

In this appendix we follow Martini & Weinberg (2001), and provide some essential formulae to compute the quasar lifetime t_Q and duty cycle using the measured correlation length and quasar number density.

The Martin-Weinberg model is very sensitive to the halo number density at the high-mass end, and hence a more suitable fitting function is needed. The Press & Schechter (1974; PS) halo number density as a function of halo mass M and redshift is given by

$$n(M, z)\,dM = -\sqrt{\frac{2}{\pi}}\frac{\rho_0}{M}\frac{\delta_c(z)}{\sigma^2(M)}\frac{d\sigma(M)}{dM}\exp\left(-\frac{\delta_c^2(z)}{2\sigma^2(M)}\right)dM, \quad \text{(C1)}$$

[20] See http://www.sdss.org/dr5.
[21] See http://casa.colorado.edu/~ajsh/mangle.

where $\rho_0 = 2.78 \times 10^{11} \Omega_M\ h^2\ M_\odot\ \mathrm{Mpc}^{-3}$ is the mean density of the universe at $z = 0$; $\sigma(M)$ is the current ($z = 0$) rms linear density fluctuation smoothed by a spherical top hat with radius $r = (3M/4\pi\rho_0)^{1/3}$, normalized by σ_8; and $\delta_c(z) = \delta_{c,0}/D(z)$ is the threshold density for collapse of a homogeneous spherical perturbation at redshift z, with $D(z)$ the growth factor and $\delta_{c,0}$ the critical threshold at $z = 0$, given in Appendix A of Navarro et al. (1997). The Sheth-Tormen (ST) halo mass function is (Sheth & Tormen 1999)

$$n(M,\ z)\,dM = -A\sqrt{\frac{2a}{\pi}}\frac{\rho_0}{M}\frac{\delta_c(z)}{\sigma^2(M)}\frac{d\sigma(M)}{dM} \times \left\{1 + \left[\frac{\sigma^2(M)}{a\delta_c^2(z)}\right]^p\right\}\exp\left(-\frac{a\delta_c^2(z)}{2\sigma^2(M)}\right)dM, \tag{C2}$$

where $A = 0.3222$, $a = 0.707$, and $p = 0.3$. We compared the ST and PS formalism using the $z = 3$ and $z = 4$ outputs of a cosmological N-body simulation generated from the TPM code of P. Bode and J. P. Ostriker (Bode et al. 2000; Bode & Ostriker 2003), which assumed the *WMAP* year 3 cosmology ($\Omega_m = 0.26$, $\Omega_\Lambda = 0.74$, $H_0 = 72$ km s^{-1} Mpc^{-1}, spectral index $n_s = 0.95$, and $\sigma_8 = 0.77$). The simulation included $\sim 10^9$ particles in a box 1000 comoving h^{-1} Mpc on a side; the mass per particle was $6.72 \times 10^{10}\ h^{-1}\ M_\odot$. Dark matter halos were identified with the friends-of-friends algorithm using a linking parameter one-fifth of the mean interparticle separation of the simulation. We found that the mass function in the simulations for $M > 2 \times 10^{12}\ h^{-1}\ M_\odot$ followed the ST predictions closely, while the PS form increasingly underpredicted the simulations at large masses, in agreement with a number of other authors (e.g., Sheth & Tormen 1999; Jenkins et al. 2001; Heitmann et al. 2006). Therefore we use the ST formula for the halo mass function throughout the paper.

The rms density fluctuation at $z = 0$, $\sigma(M)$, is given by

$$\sigma(M) = \left[\frac{1}{2\pi^2}\int_0^\infty dk\, k^2 P(k)\tilde{W}^2(kr)\right]^{1/2}, \tag{C3}$$

where $\tilde{W} = 3(\sin kr - kr\cos kr)/(kr)^3$ is the filter function for a spherical top hat. The CDM power spectrum $P(k) \propto k^{n_s}T^2(k)$, where n_s is the primeval inflationary power spectrum index and $T(k)$ is the transfer function given by (Bardeen et al. 1986)

$$T(k) = \frac{\ln(1 + 2.34q)}{2.34q} \times [1 + 3.89q + (16.1q)^2 + (5.46q)^3 + (6.71q)^4]^{-1/4}, \tag{C4}$$

where $q = k/\Gamma$ and Γ is the CDM shape parameter (with units of h Mpc^{-1}), given approximately by $\Gamma = \Omega_M h \exp(-\Omega_b - (2h)^{1/2}\Omega_b/\Omega_M)$ (Sugiyama 1995). Using this CDM power spectrum we numerically integrate equation (C3) to obtain $\sigma(M)$ and $d\sigma(M)/dM$. The rms fluctuation at redshift z is thus given by

$$\sigma(M,\ z) = \sigma(M)D(z), \tag{C5}$$

from which we can define a characteristic mass scale M_* such that $\sigma(M_*(z)) = \delta_c(z)$.

The halo lifetime is defined to be the median interval before a halo with initial mass M becomes a halo with mass $M_2 = 2M$ via mergers. This condition is given in Lacey & Cole (1993),

$$P(S < S_2,\ \omega_2 \mid S_1,\ \omega_1) = \frac{1}{2}\frac{\omega_1 - 2\omega_2}{\omega_1}\exp\left(\frac{2\omega_2(\omega_1 - \omega_2)}{S_1}\right) \times \mathrm{erfc}\left(\frac{S_2(\omega_1 - 2\omega_2) + S_1\omega_2}{\sqrt{2S_1S_2(S_1S_2)}}\right) + \frac{1}{2}\mathrm{erfc}\left(\frac{S_1\omega_2 - S_2\omega_1}{\sqrt{2S_1S_2(S_1 - S_2)}}\right) = 0.5, \tag{C6}$$

where $S_1 = \sigma^2(M)$, $S_2 = \sigma^2(2M)$, $\omega_1 = \delta_c(z)$, and $\omega_2 = \delta_c(z_2)$. Hence the halo lifetime is given by $t_H(M,\ z) = t_U(z_2) - t_U(z)$, where $t_U(z)$ the age of the universe at redshift z, and z_2 is solved numerically from equation (C6). For comparison, the age of the universe at $z = 3.5$ is ~ 2 Gyr.

Halos with mass $> M_*$ are more strongly clustered than the underlying distribution of mass; the bias factor $b(M,\ z)$ of halos with mass M at redshift z is given by (Jing 1998)

$$b(M,\ z) = \left\{1 + \frac{1}{\delta_{c,0}}\left[\frac{\delta_c^2(z)}{\sigma^2(M)} - 1\right]\right\}\left[\frac{\sigma^4(M)}{2\delta_c^4(z)} + 1\right]^{(0.06 - 0.02n_{\mathrm{eff}})}, \tag{C7}$$

where $n_{\mathrm{eff}} = -3 - 6(d\ln\sigma/d\ln M)$ is the effective index of the power spectrum on a mass scale M. The effective bias factor for all halos with mass above the minimal mass M_{min} is therefore

$$b_{\mathrm{eff}}(M_{\mathrm{min}},\ z) = \int_{M_{\mathrm{min}}}^\infty dM\,\frac{b(M,\ z)n(M,\ z)}{t_H(M,\ z)}\left[\int_{M_{\mathrm{min}}}^\infty dM\,\frac{n(M,\ z)}{t_H(M,\ z)}\right]^{-1}. \tag{C8}$$

Since $n(M,\ z)$ drops rapidly with increasing mass, b_{eff} is only slightly larger than $b(M_{\mathrm{min}},\ z)$. We have tested equations (C7) and (C8) with the simulations described above. We find that they correctly predict the bias inferred from the integrated correlation function ξ_{20}. In particular, at the two output redshifts of the simulations, $z = 3$ and $z = 4$, the simulation results give a bias factor (calculated from the ratio of ξ_{20} for the halos and for the dark matter) of 6.2 at $z = 3$ and 10.2 at $z = 4$, for halos with mass $\geq 2 \times 10^{12}\ h^{-1}\ M_\odot$, while the analytical bias formalism gives $b_{\mathrm{eff}} = 7.3$ and 10.7, respectively. This difference is negligible when we integrate over a wide redshift range (eq. [C11]) and compared with other uncertainties. On the other hand, there is clear evidence for a scale-dependent bias, which we plan to explore further in future work.

The model-predicted quasar correlation function $\xi_{\mathrm{model}}(r,\ z)$ is therefore

$$\xi_{\mathrm{model}}(r,\ z) = b_{\mathrm{eff}}^2\xi_m(r,\ z) = b_{\mathrm{eff}}^2\xi_m(r)D^2(z), \tag{C9}$$

where $D(z)$ is the linear growth factor of fluctuations and $\xi_m(r)$ is the present-day mass correlation function, defined as

$$\xi_m(r) = \frac{1}{2\pi^2}\int_0^\infty dk\, k^2 P(k)\frac{\sin kr}{kr}, \tag{C10}$$

normalized using σ_8. Comparison of $\xi_m(r,\ z)$ with the mass correlation function from the cosmological N-body simulation mentioned above at $z = 3$ and $z = 4$ shows quite good agreement.

The correlation function we have actually measured is averaged over a certain redshift range, hence

$$\bar{\xi}(r) = \frac{\int dV_c\, n^2_{\rm QSO}(z)\xi_{\rm model}(r,\ z)}{\int dV_c\, n^2_{\rm QSO}(z)}, \qquad \text{(C11)}$$

where $n_{\rm QSO}(z) = \Phi(z)f(z)$ is the *observed* quasar number density, i.e., the actual quasar number density times the complicated selection function $f(z)$, and dV_c is the differential comoving volume element, given in Hogg (1999); $n_{\rm QSO}$ is computed using our full high-redshift clustering subsample (see Fig. 2). Note that the above equation is only valid for scales r over which $n_{\rm QSO}$ is nearly constant and ξ does not significantly evolve over the time, $r/[(1+z)c]$ (PMN04). For our selected range $[r_{\rm min},\ r_{\rm max}] = [5,\ 20]\ h^{-1}$ Mpc, these conditions are satisfied.

REFERENCES

Abazajian, K., et al. 2003, AJ, 126, 2081
———. 2005, AJ, 129, 1755
Adelberger, K. L., Erb, D. K., Steidel, C. C., Reddy, N. A., Pettini, M., & Shapley, A. E. 2005a, ApJ, 620, L75
Adelberger, K. L., Steidel, C. C., Pettini, M., Shapley, A. E., Reddy, N. A., & Erb, D. K. 2005b, ApJ, 619, 697
Adelberger, K. L., et al. 1998, ApJ, 505, 18
Adelman-McCarthy, J. K., et al. 2006, ApJS, 162, 38
———. 2007, ApJS, submitted
Ajiki, M., et al. 2006, PASJ, 58, 499
Allen, P. D., Moustakas, L. A., Dalton, G., MacDonald, E., Blake, C., Clewley, L., Heymans, C., & Wegner, G. 2005, MNRAS, 360, 1244
Anderson, S. F., et al. 2003, AJ, 126, 2209
Babich, D., & Loeb, A. 2006, ApJ, 640, 1
Bardeen, J., Bond, J. R., Kaiser, N., & Szalay, A. S. 1986, ApJ, 304, 15
Basilakos, S., Georgakakis, A., Plionis, M., & Georantopoulos, I. 2004, ApJ, 607, L79
Blanton, M. R., et al. 2000, ApJ, 531, 1
———. 2003, AJ, 125, 2276
———. 2005, AJ, 129, 2562
Bode, P., & Ostriker, J. P. 2003, ApJS, 145, 1
Bode, P., Ostriker, J. P., & Xu, G. 2000, ApJS, 128, 561
Cohen, J. G., et al. 1996, ApJ, 471, L5
Colless, M., et al. 2001, MNRAS, 328, 1039
Croom, S. M., & Shanks, T. 1996, MNRAS, 281, 893
Croom, S. M., et al. 2004, MNRAS, 349, 1397
———. 2005, MNRAS, 356, 415
da Ângela, J., et al. 2005, MNRAS, 360, 1040
Davis, M., & Peebles, P. J. E. 1983, ApJ, 267, 465
Djorgovski, S. 1991, in ASP Conf. Ser. 21, The Space Distribution of Quasars, ed. D. Crampton (San Francisco: ASP), 349
Djorgovski, S. G., Stern, D., Mahabal, A. S., & Brunner, R. 2003, ApJ, 596, 67
Eisenstein, D. J., et al. 2005, ApJ, 633, 560
Fan, X. 1999, AJ, 117, 2528
Fan, X., et al. 2001, AJ, 122, 2833
Ferrarese, L. 2002, ApJ, 578, 90
Fukugita, M., et al. 1996, AJ, 111, 1748
Gaskell, C. M. 1982, ApJ, 263, 79
Giavalisco, M., et al. 1998, ApJ, 503, 543
Gilli, R., et al. 2005, A&A, 430, 811
Groth, E. J., & Peebles, P. J. E. 1977, ApJ, 217, 385
Gunn, J. E., et al. 1998, AJ, 116, 3040
———. 2006, AJ, 131, 2332
Haiman, Z., & Hui, L. 2001, ApJ, 547, 27
Hamilton, A. J. S. 1993, ApJ, 417, 19
Hamilton, A. J. S., & Tegmark, M. 2004, MNRAS, 349, 115
Hawkins, E., et al. 2003, MNRAS, 346, 78
Heitmann, K., Lukic, Z., Habib, S., & Ricker, P. M. 2006, ApJ, 642, L85
Hennawi, J., et al. 2006a, AJ, 131, 1
———. 2006b, ApJ, 651, 61
Hogg, D. W. 1999, preprint (astro-ph/9905116)
Hogg, D. W., Finkbeiner, D. P., Schlegel, D. J., & Gunn, J. E. 2001, AJ, 122, 2129
Hopkins, P. F., Hernquist, L., Martini, P., Cox, J., Robertson, B., Di Matteo, T., & Springel, V. 2005, ApJ, 625, L71
Hopkins, P. F., et al. 2006, ApJ, submitted
Iovino, A., & Shaver, P. A. 1988, ApJ, 330, L13
Ivezić, Z., et al. 2004, Astron. Nachr., 325, 583
Jenkins, A., et al. 2001, MNRAS, 321, 372
Jiang, L., et al. 2006, AJ, 131, 2788
Jing, Y. P. 1998, ApJ, 503, L9
Kaiser, N. 1984, ApJ, 284, L9
———. 1986, MNRAS, 219, 785
———. 1987, MNRAS, 227, 1
Kashikawa, N., et al. 2006, ApJ, 637, 631
Kollmeier, J. A., et al. 2006, ApJ, 648, 128
Kormendy, J., & Richstone, D. 1995, ARA&A, 33, 581
Kundic, T. 1997, ApJ, 482, 631
Lacey, C., & Cole, S. 1993, MNRAS, 262, 627
La Franca, F., Andreani, P., & Cristiani, S. 1998, ApJ, 497, 529
Landy, S. D., & Szalay, A. S. 1993, ApJ, 412, 64
Lee, K.-S., et al. 2006, ApJ, 642, 63
Lidz, A., Hopkins, P. F., Cox, T. J., Hernquist, L., & Robertson, B. 2006, ApJ, 641, 41
Lupton, R., Gunn, J. E., Ivezić, Z., Knapp, G. R., & Kent, S. 2001, in ASP Conf. Ser. 238, Astronomical Data Analysis Software and Systems X, ed. F. R. Harnden, Jr., F. A. Primini, & H. E. Payne (San Francisco: ASP), 269
Lynden-Bell, D. 1969, Nature, 223, 690
Magorrian, J., et al. 1998, AJ, 115, 2285
Martini, P. 2004, in Coevolution of Black Holes and Galaxies, ed. L. C. Ho (Cambridge: Cambridge Univ. Press), 406
Martini, P., & Weinberg, D. H. 2001, ApJ, 547, 12
Meneux, B., et al. 2006, A&A, 452, 387
Mushotzky, R. 2004, in Supermassive Black Holes in the Distant Universe, ed. A. J. Barger (Dordrecht: Kluwer), 53
Myers, A. D., et al. 2006, ApJ, 638, 622
———. 2007a, ApJ, 658, 85
———. 2007b, ApJ, 658, 99
Navarro, J. F., Frenk, C. S., & White, S. D. M. 1997, ApJ, 490, 493
Osmer, P. S. 1981, ApJ, 247, 762
Ouchi, M., et al. 2005, ApJ, 635, L117
Percival, W., et al. 2007, ApJ, 657, 645
Pier, J. R., et al. 2003, AJ, 125, 1559
Plionis, M. 2007, in Proc. 26th Moriond Astrophysics Meeting, ed. L. Tresse, S. Maurogordato, & J. Trân Thanh Vân (Gif sur Yvette: Editions Frontières), in press (astro-ph/0607324)
Porciani, C., Magliocchetti, M., & Norberg, P. 2004, MNRAS, 355, 1010 (PMN04)
Porciani, C., & Norberg, P. 2006, MNRAS, 371, 1824
Press, W. H., & Schechter, P. 1974, ApJ, 187, 425
Puccetti, S., et al. 2006, A&A, 457, 501
Quadri, R., et al. 2006, ApJ, 654, 138
Richards, G. T., et al. 2002a, AJ, 123, 2945
———. 2002b, AJ, 124, 1
———. 2006, AJ, 131, 2766
Roukema, B. F., Mamon, G. A., & Bajtlik, S. 2002, A&A, 382, 397
Salpeter, E. E. 1964, ApJ, 140, 796
Schlegel, D. J., Finkbeiner, D. P., & Davis, M. 1998, ApJ, 500, 525
Schneider, D. P., Schmidt, M., & Gunn, J. E. 1994, AJ, 107, 1245
Schneider, D. P., et al. 2000, AJ, 120, 2183
———. 2005, AJ, 130, 367
———. 2006, AJ, submitted
Scranton, R., et al. 2005, ApJ, 633, 589
Serber, W., Bahcall, N., Ménard, B., & Richards, G. 2006, ApJ, 643, 68
Shaver, P. A. 1984, A&A, 136, L9
Shen, Y., et al. 2007, ApJ, 654, L115
Sheth, R. K., & Tormen, G. 1999, MNRAS, 308, 119
Smith, J. A., et al. 2002, AJ, 123, 2121
Spergel, D. N., et al. 2003, ApJS, 148, 175
———. 2007, ApJ, in press (astro-ph/0603449)
Steidel, C. C., et al. 1998, ApJ, 492, 428
Stephens, A. W., Schneider, D. P., Schmidt, M., Gunn, J. E., & Weinberg, D. H. 1997, AJ, 114, 41
Stiavelli, M., et al. 2005, ApJ, 622, L1
Stoughton, C., et al. 2002, AJ, 123, 485
SubbaRao, M., Frieman, J., Bernardi, M., Loveday, J., Nichol, B., Castander, F., & Meiksin, A. 2002, Proc. SPIE, 4847, 452
Sugiyama, N. 1995, ApJS, 100, 281
Tegmark, M., & Peebles, P. J. E. 1998, ApJ, 500, L79

Tegmark, M., et al. 2004, ApJ, 606, 702
———. 2006, Phys. Rev. D, 74, 123507
Totsuji, H., & Kihara, T. 1969, PASJ, 21, 221
Tremaine, S., et al. 2002, ApJ, 574, 740
Tucker, D. L., et al. 2006, Astron. Nachr., 327, 821
Tytler, D., & Fan, X. 1992, ApJS, 79, 1
Vanden Berk, D. E., et al. 2001, AJ, 122, 549
Weinberg, D. H., Davé, R., Katz, N., & Hernquist, L. 2004, ApJ, 601, 1
Weymann, R. J., Morris, S. L., Foltz, C. B., & Hewett, P. C. 1991, ApJ, 373, 23
York, D. G., et al. 2000, AJ, 120, 1579
Yu, Q., & Tremaine, S. 2002, MNRAS, 335, 965
Zehavi, I., et al. 2004, ApJ, 608, 16
———. 2005, ApJ, 630, 1